Photophysical and Photobiological Properties of Dinuclear Iridium(III) Bis-tridentate Complexes

Bingqing Liu[†], **Susan Monro**[‡], **Levi Lystrom**[†], **Colin G. Cameron**[§], **Katsuya Colon**[§], **Huimin Yin**[‡], **Svetlana Kilina**[†], **Sherri A. McFarland**[*,‡,§], and **Wenfang Sun**[*,†]

[†]Department of Chemistry and Biochemistry, North Dakota State University, Fargo, ND 58108-6050, USA

[‡]Department of Chemistry, Acadia University, 6 University Avenue, Wolfville, NS B4P 2R6, Canada

[§]Department of Chemistry and Biochemistry, University of North Carolina at Greensboro, Greensboro, NC 27402-6170, USA

Abstract

A series of cationic dinuclear iridium(III) complexes (**Ir1** - **Ir5**) bearing terpyridine-capped fluorenyl bridging ligand and different polypyridyl or cyclometalating terminal tridentate ligands were synthesized, characterized, and evaluated for their photophysical and photobiological activities. The influence of the bridging and terminal ligands on the photophysical properties of the complexes was investigated by UV-vis absorption, emission, and transient absorption spectroscopy, and simulated by TDDFT calculations. All of the complexes displayed strong bridging-ligand localized visible $^1\pi,\pi^*$ absorption and red- or near-infrared (NIR) phosphorescence as well as broad triplet excited-state absorption across both visible and NIR wavelengths. These triplet states were assigned as predominantly $^3\pi,\pi^*$ for **Ir1** ($\tau = 3.1$ μs) and **Ir4** ($\tau = 48$ μs), and predominantly ^{3}CT (charge transfer) for **Ir2**, **Ir3** and **Ir5** ($\tau = 1.7$–2.7 μs). Complexes **Ir1** – **Ir5** acted as *in vitro* photodynamic therapy (PDT) agents toward human SK-MEL-28 melanoma cells when activated with visible light, with submicromolar photocytotoxicity and phototherapeutic indices (PIs) ranging from 20 to almost 300. The *in vitro* PDT effects with visible light did not correlate with singlet oxygen ($^1O_2$) quantum yields or DNA photocleaving capacity probed under cell-free conditions. All of the Ir(III) complexes phosphoresced brightly when associated with compromised cells (with or without a light treatment) and exhibited photoactivated cellular uptake, highlighting the theranostic potential of this new class of Ir(III) complex photosensitizers.

[*]**Corresponding Author**: Wenfang.Sun@ndsu.edu. Telephone: 701-231-6254. Fax: 701-231-8831. samcfarl@uncg.edu. Telephone: 336-256-1080. Fax: 336-334-5402.

Graphical Abstract

Dinuclear iridium(III) complexes bearing terpyridine-capped fluorenyl bridging ligand and different polypyridyl or cyclometalating terminal tridentate ligands exhibited *in vitro* photodynamic therapeutic effects toward SK-MEL-28 melanoma cells upon visible light activation, with submicromolar photocytotoxicity and phototherapeutic indices ranging from 20 to almost 300. They phosphoresced brightly when associated with compromised cells and exhibited photoactivated cellular uptake, highlighting the theranostic potential of these complexes. Both the bridging and terminal ligands impacted the photophysical and photobiological activities significantly.
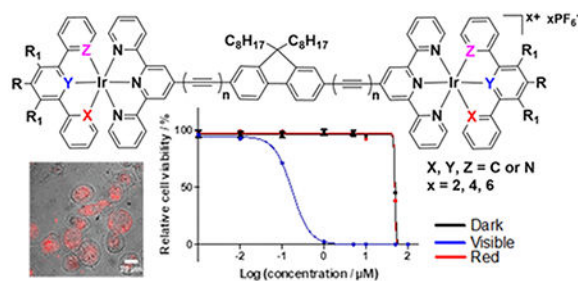
INTRODUCTION

In recent decades transition-metal complexes have come to the forefront in the search for new chemical entities in drug discovery and biological chemistry.[1] Platinum (Pt)-based metal complexes have been investigated extensively for cancer therapy,[2] with cisplatin being arguably the most successful anticancer drug to date. Nevertheless, there is continued focus on developing alternatives to cisplatin[3,4] and other nonselective cytotoxic agents in an effort to reduce the systemic side effects associated with conventional chemotherapy approaches. Ruthenium (Ru)-containing compounds have been widely studied as alternatives to the Pt-derived drugs, with a few (*e.g.,* NAMI-A, KP1019, and IT-139) entering clinical trials[5–7] but none in the clinic to date. With selectivity being a key consideration for any new drug, Ru(II) coordination complexes and other transition-metal complexes are also being considered for targeted modalities such as photodynamic therapy (PDT).[8–11]

PDT has been known for over a hundred years[12] yet remains underexploited in mainstream cancer therapy despite its precise spatiotemporal selectivity. In its narrowest definition, PDT involves activation of an otherwise nontoxic photosensitizer with photons of appropriate energy to produce a triplet excited state that can relax through singlet oxygen ($^1O_2$) sensitization or the production of other reactive oxygen species (ROS).[13] Collectively, cytotoxic ROS destroy tumors and tumor vasculature, and can even invoke an antitumor immune response under the right conditions. Porphyrin-based organic compounds (and the related chlorins, bacteriochlorins, and phthalocyanines) have traditionally served as ROS-generating photosensitizers for PDT.[14,15] However, transition-metal complex photosensitizers have the potential to both (i) expand the scope of PDT to include oxygen-independent mechanisms of action, and thus improve PDT efficacy in hypoxic tissue, and (ii) broaden the wavelength range that can be used to include deeper tissue-penetrating near-

infrared (NIR) light. One recent example is our Ru(II) complex TLD1433,[16] currently in clinical trials for treating bladder cancer with PDT (ClinicalTrials.gov Identifier: NCT03053635), and its transferrin conjugate Rutherrin™.[17]

TLD1433 incorporates a special π-expansive ligand derived from imidazo[4,5-f] [1,10]phenanthroline appended to an α-terthienyl unit, which imparts a long-lived triplet intraligand excited state (^{3}IL) of significant π,π^* character that is lower in energy than the triplet metal-to-ligand charge transfer (^{3}MLCT) state that typically dominates the photophysical dynamics of Ru(II) polypyridyl complexes. The reduced intersystem crossing (ISC) rates characteristic of spin-forbidden $^3\pi,\pi^*$ transitions centered on the organic moiety are responsible for the much longer intrinsic triplet lifetimes in these constructs that are known as metal-organic dyads.[18,19] The implication is that slow ISC back to the ground state from ^{3}IL states provides ample opportunity for requisite bimolecular processes that constitute the phototoxic effects of PDT. We have demonstrated very potent *in vitro* PDT effects from a variety of Ru(II) dyads with low-lying, long-lived ^{3}IL states, including both contiguously-fused π-extended azaaromatic ligands[20] as well as ligands tethered to π-extended aromatic chromophores.[16,21–23] More recently, we have incorporated π-expansive ligands into Ir(III) metal complexes to extend intrinsic excited state lifetimes for both reverse saturable absorption (RSA) and PDT applications.[24,25]

Compared to the large number of Ru(II) systems that have been explored, investigations on Ir(III) complexes for *in vitro* PDT have been emerged in recent years.[24–44] While Ir(III) complexes derived from diimine ligands (N^N) may fall short of the optimal absorption window for PDT, we have demonstrated that incorporation of two cyclometalating ligands (C^N) to form biscyclometalated Ir(III) complexes extends the ground-state absorption spectrum significantly, and that installation of a π-extended N^N ligand alongside the two C^N ligands extends the lifetime through population of ^{3}IL states. The result is nanomolar PDT potency with phototherapeutic indices (PIs) greater than 400.[25] We also showed that it was possible to use π-extended C^N ligands without compromising the potent *in vitro* PDT effects in Ir(III)-based systems that act as near-infrared-emitting theranostic agents.[24]

The large luminescence quantum yields for certain Ir(III) complexes combined with their high yields for triplet state formation and good photostability make these metal complexes very attractive for photobiological applications such as PDT. In addition, their excitation and emission energies, as well as other photophysical and biological/chemical properties, can be systematically tuned via minor structural changes to a highly versatile and modular architecture. Despite these attributes, Ir(III) complexes studied to date[30] still fall short of some of the best Ru(II)-based *in vitro* PDT agents. The purpose of the present study is to use rational design principles to improve the water-solubility and *in vitro* PDT effects within the Ir(III) class of photosensitizers. Specifically, installing two Ir(III) centers in a single complex might simultaneously amplify photocytotoxicity and increase water solubility.

The solubility of organometallic complexes in aqueous solution can be improved by increasing the number of charges in the complex, which should be applicable to multinuclear iridium(III) complexes with C^N and/or N^N ligands.[45] Since the photophysical and biological properties of metal complexes bearing tridentate ligand(s) can be readily tuned by

modification of the 4′-position of the tridentate ligand(s), and because the bis-tridentate ligand coordination prevents the formation of stereoisomers upon complexation with transition metals, tridentate ligands are chosen for this Ir(III) study.[46,47] Our previous work with bis-terpyridyl dinuclear Pt(II) complexes showed that the fluorenyl bridging group imparted these systems with intense absorption in the visible region (400-500 nm) and reasonably long-lived triplet excited states.[48] These desirable properties led us to investigate fluorenyl-linked Ir(III) systems as *in vitro* PDT agents.

Herein, we report the synthesis, characterization, and photophysical/photobiological properties of stable dinuclear Ir(III) complexes (Chart 1) of +2, +4, or +6 charges, with the charge determined by the identities of the metal coordinating atoms of different terminal tridentate ligands. Fluorene was chosen as the central bridging group for the two Ir-tpy components because it is a rigid π-conjugated linker expected to enhance molar extinction coefficients in the visible spectral region. Complexes **Ir1** and **Ir3** – **Ir5** incorporate 9,9-dioctyl-2,7-di(terpyridyl)-9*H*-fluorene (**L1**) as the bridging ligand, with variation at the terminal tridentate ligands: 4′-phenyl-2,2′:6′,2″-terpyridine (N^N^N), 1,3-dipyridyl-4,6-dimethylbenzene (N^C^N), 4,6-diphenyl-2,2′-bipyridine (C^N^N), or 2,4,6-triphenyl-pyridine (C^N^C). Complex **Ir2** uses 9,9-dioctyl-2,7-bis(2-phenylethynyl)-9*H*-fluorene (**L2**) as the bridging ligand to extend the π-conjugation length, which is anticipated to facilitate intraligand charge transfer (ILCT) transitions that fall in the PDT window and to also increase visible wavelength absorption.

EXPERIMENTAL SECTION

Synthesis and Characterizations.

Chemicals and solvents were purchased from Sigma-Aldrich or Alfa Aesar and used as received unless otherwise noted. The bridging ligands (**L1** and **L2**) were synthesized following our previously reported procedures.[48] 4′-Phenyl-2,2′:6′,2″-terpyridine (N^N^N),[49] 1,3-dipyridyl-4,6-dimethylbenzene (N^C^N),[50] 4,6-diphenyl-2,2′-bipyridine (C^N^N),[51] 2,4,6-triphenylpyridine (C^N^C),[52] 4′-phenyl-2,2′:6′,2″-terpyridine-IrCl₃ (N^N^N-IrCl₃),[53] and {[1,3-dipyridyl-4,6-dimethylbenzene]IrCl₂}₂ (N^C^N Ir-dimer)[54] were synthesized according to established methods. Silica gel (60 Å, 230–400 mesh) and Al_2O_3 (activated, neutral) were purchased from Sorbent Technology. Complexes **Ir1** – **Ir5** were characterized by ^{1}H NMR, high resolution electrospray ionization mass spectrometry (ESI–MS), and elemental analysis. ^{1}H NMR spectra were recorded on Bruker-400 or Varian Oxford–500 spectrometers. ESI–MS analyses were collected using a Waters Synapt G2-Si Mass Spectrometer. Elemental analyses were performed by NuMega Resonance Laboratories, Inc. (San Diego, California). The synthetic schemes for complexes **Ir1** – **Ir5** are outlined in Scheme 1.

L1-(IrCl₃)₂.—**L1** (170.5 mg, 0.2 mmol) and $IrCl_3$ 3H₂O (141 mg, 0.4 mmol) were combined in degassed ethylene glycol (15 mL) and heated to 160 °C with protection from light. After 30 min, the reaction mixture was cooled to room temperature and filtered. The resulting precipitate was washed with ethanol, water, and diethyl ether to give ***Ll-Ir(Cl₃)₂*** as a red solid (254 mg, 88%). ^{1}H NMR (500 MHz, *d*⁶-DMSO) δ 9.27 (d, *J* = 5.0 Hz, 4H), 9.18

(t, J = 8.8 Hz, 4H), 9.06 (dd, J = 11.3, 3.0 Hz, 2H), 8.98 – 8.94 (m, 2H), 8.70 (t, J = 9.8 Hz, 2H), 8.52 (dd, J = 8.2, 4.1 Hz, 2H), 8.38 (t, J = 7.8 Hz, 4H), 8.32 (d, J = 8.5 Hz, 2H), 8.06 – 8.01 (m, 4H), 2.43 (m, 4H), 0.95 – 0.69 (m, 20H), 0.48 (m, 10H).

Ir1.—4′-Phenylterpyridine-IrCl$_3$ (60.7 mg, 0.1 mmol) and **L1** (42.6 mg, 0.05 mmol) were combined in degassed ethylene glycol (10 mL) and heated to 196 °C with protection from light. After 2 h, the reaction mixture was cooled to room temperature, and saturated NH$_4$PF$_6$ aqueous solution (20 mL) was added to precipitate the product. The crude material was purified by column chromatography on alumina gel. Unreacted ligand was eluted first with CH$_2$Cl$_2$, followed by elution of the desired product with an acetone/water gradient (100:0 to 95:5 (v/v)). The product was a yellow solid (60 mg, 65%). ^{1}H NMR (400 MHz, d^6-DMSO) δ 9.76 (s, 4H), 9.67 (s, 4H), 9.50 – 9.34 (m, 4H), 9.29 (d, J = 8.2 Hz, 4H), 9.05 (s, 2H), 8.88 – 8.78 (m, 2H), 8.53-8.39 (m, 14H), 8.17 – 7.93 (m, 8H), 7.87 (t, J = 7.6 Hz, 4H), 7.78 (t, J = 7.4 Hz, 2H), 7.62 (dd, J = 12.2, 5.8 Hz, 8H), 2.61 (m, 4H), 0.89 (m, 20H), 0.62 (m, 10H). ESI-HRMS (m/z, in acetone): calcd. for $[C_{101}H_{90}Ir_2N_{12}]^{6+}$, 309.4445; found, 309.4446. Calcd. for $[C_{101}H_{90}Ir_2N_{12}PF_6]^{5+}$, 400.3262; found, 400.3270. Calcd. for $[C_{101}H_{90}Ir_2N_{12}P_2F_{12}]^{4+}$, 536.6489; found, 536.6503. Anal. Calcd. (%) for C$_{101}$H$_{90}$F$_{36}$Ir$_2$N$_{12}$P$_6$·6H$_2$O: C, 42.80; H, 3.63; N, 5.93. Found: C, 42.61; H, 3.74; N, 5.98.

Ir2.—4′-Phenylterpyridine-IrCl$_3$ (60.7 mg, 0.1 mmol), **L2** (45 mg, 0.05 mmol), and AgOTf (77 mg, 0.3 mmol) were combined in degassed ethylene glycol (10 mL) and heated to 196 °C with protection from light. After 24 h, the mixture was cooled to room temperature, and saturated NH$_4$PF$_6$ aqueous solution (20 mL) was added to precipitate the product. The crude material was purified by column chromatography on alumina gel. Unreacted ligand was eluted with CH$_2$Cl$_2$ first, followed by elution of the desired product using an acetone/water gradient (100:0 to 95:5 (v/v)). The purified product was a dark red powder (37 mg, 24%). ^{1}H NMR (400 MHz, d^6-DMSO) δ 9.62 (t, J = 7.0 Hz, 6H), 9.22 (m, 8H), 8.48 (m, 6H), 8.32 (m, 8H), 7.92 (m, 8H), 7.77 (m, 6H), 7.71 (m, 4H), 7.51 (m, 10H), 2.51 (m, 4H), 1.02 (m, 20H), 0.67 (m, 10H). ESI-HRMS (m/z, in acetone): calcd. for $[C_{105}H_{90}Ir_2N_{12}]^{6+}$, 317.4445; found, 317.4442. Anal. Calcd. (%) for C$_{105}$H$_{90}$F$_{36}$Ir$_2$N$_{12}$P6·13H$_2$O·CH$_2$Cl$_2$: C, 41.16; H, 3.85; N, 5.43. Found: C, 40.83; H, 3.47; N, 5.44.

Ir3.—{[2,2′-(4,6-Dimethyl-1,3-phenylene)bis-pyridine]IrCl$_2$}$_2$ (72 mg, 0.069 mmol) and **L1** (59 mg, 0.069 mmol) were heated in degassed ethylene glycol (10 mL) at 196 °C with protection from light. After 1 h, the reaction mixture was added to water (10 mL) and filtered. Saturated NH$_4$PF$_6$ aqueous solution (20 mL) was added to the filtrate, and the resulting yellow precipitate was collected by centrifugation, washed with water (3×10 mL), and dried under vacuum. The crude product was purified by column chromatography on alumina gel. Unreacted ligand was eluted first with CH$_2$Cl$_2$, followed by elution of the desired product with an acetone/water gradient (100:0 to 95:5 (v/v)). The pure product was a yellow solid (94 mg, 58%). ^{1}H NMR (400 MHz, d^6-DMSO) δ 9.65 (td, J = 5.0, 2.5 Hz, 4H), 9.18 (t, J = 9.9 Hz, 4H), 8.90 (m, 2H), 8.71 (m, 2H), 8.47 (dd, J = 9.6, 2.6 Hz, 2H), 8.37 (d, J = 8.4 Hz, 4H), 8.30 (dd, J = 8.8, 4.6 Hz, 4H), 7.99 (ddd, J = 7.5, 5.9, 2.7 Hz, 4H), 7.77 (m, 2H), 7.68 (ddd, J = 9.7, 4.8, 2.7 Hz, 4H), 7.52 (ddd, J = 6.7, 4.1, 1.2 Hz, 4H), 7.45 (dd, J = 5.7, 1.8 Hz, 2H), 7.40 (s, 2H), 7.12 (ddd, J = 8.4, 6.5, 1.7 Hz, 4H), 2.93 (s, 12H), 2.52 (m,

4H), 0.90 (m, 20H), 0.62 (m, 10H). ESI-HRMS (m/z, in acetone): calcd. for $[C_{95}H_{90}Ir_2N_{10}]^{4+}$, 439.1652; found, 439.1668. Calcd. for $[C_{95}H_{90}Ir_2N_{10}PF_6]^{3+}$, 633.8750; found, 633.8768. Anal. Calcd. (%) for $C_{95}H_{90}F_{24}Ir_2N_{10}P_45H_2O$: C, 47.03; H, 4.15; N, 5.77. Found: C, 46.97; H, 4.32; N, 5.98.

Ir4.—L1-(IrCl$_3$)$_2$ (72.4 mg, 0.05 mmol), 4,6-diphenyl-2,2′-bipyridine (30.8 mg, 0.1 mmol), and AgOTf (77 mg, 0.3 mmol) were mixed in degassed ethylene glycol (10 mL) and heated to 196 °C with protection from light. After 24 h, the mixture was cooled to room temperature, and saturated NH$_4$PF$_6$ aqueous solution (20 mL) was added to precipitate the crude product, which was purified by column chromatography on alumina gel. Unreacted ligand was eluted first with CH$_2$Cl$_2$,, followed by elution of the desired product with an acetone/water gradient (100:0 to 95:5 (v/v)). The pure product was a yellow solid (38 mg, 41%). ^{1}H NMR (400 MHz, d^6-acetone) δ 10.05 (d, J = 7.2 Hz, 2H), 9.49 (d, J = 8.4 Hz, 2H), 9.30 (s, 2H), 9.00 (d, J = 15.3 Hz, 4H), 8.95 – 8.77 (m, 6H), 8.71 (s, 2H), 8.48 (dd, J = 18.4, 9.5 Hz, 8H), 8.36 (s, 2H), 8.28 (d, J = 6.3 Hz, 2H), 8.13 – 7.97 (m, 4H), 7.86 (dd, J = 10.8, 6.6 Hz, 4H), 7.75 (s, 2H), 7.61 (s, 6H), 7.48 – 7.33 (m, 2H), 7.19 (dd, J = 13.3, 4.5 Hz, 4H), 6.91 – 6.69 (m, 4H) 2.41 (m, 4H), 0.86 (m, 20H), 0.55 (m, 10H). ESI-HRMS (m/z, in acetone): calcd. for $[C_{103}H_{90}Ir_2N_{10}PF_6]^{3+}$, 655.8756; found, 655.8798. Anal. Calcd. (%) for $C_{103}H_{90}F_{24}Ir_2N_{10}P4·9H_2O$: C, 47.69; H, 4.20; N, 5.40. Found: C, 47.56; H, 4.46; N, 5.25.

Ir5.—L1-(IrCl$_3$)$_2$ (72.4 mg, 0.05 mmol), 2,4,6-triphenylpyridine (30.7 mg, 0.1 mmol), and AgOTf (77 mg, 0.3 mmol) were combined in degassed ethylene glycol (10 mL) and heated to 196 °C with protection from light. After 24 h, the mixture was cooled to room temperature, and saturated NH$_4$PF$_6$ aqueous solution (20 mL) was added to precipitate the crude product. The pure product was obtained by column chromatography on alumina gel. Unreacted ligand was eluted first with CH$_2$Cl$_2$,, followed by elution of the desired product with an acetone/water gradient elution (100:0 to 95:5 (v/v)). The pure product was a red solid (16 mg, 8%). ^{1}H NMR (400 MHz, d^6-DMSO) δ 9.56 (s, 4H), 9.19 – 9.09 (m, 4H), 8.95 – 8.85 (m, 4H), 8.60 (s, 4H), 8.33 (d, J = 6.6 Hz, 8H), 8.22 (s, 6H), 7.89 (s, 4H), 7.73 (s, 4H), 7.64 (s, 2H), 7.45 (s, 4H), 6.99 (s, 4H), 6.74 (s, 4H), 6.21 (s, 4H), 2.52 (m, 4H), 0.85 (m, 20H), 0.55 (m, 10H). ESI-HRMS (m/z, in acetone): calcd. for $[C_{105}H_{90}Ir_2N_8]^{2+}$, 924.3283; found, 924.3291. Anal. Calcd. (%) for $C_{105}H_{90}F_{12}Ir_2N_8P_2·0.6CH_2Cl_2$: C, 57.94; H, 4.20; N, 5.12. Found: C, 57.92; H, 3.96; N, 5.27.

Photophysical Studies.

Spectrophotometric grade solvents were purchased from Alfa Aesar. The UV–vis absorption spectra of complexes **Ir1 – Ir5** were collected on a Varian Cary 50 spectrophotometer, and steady-state emission measurements were carried out using a HORIBA FluoroMax 4 fluorometer/phosphorometer. The emission quantum yields of complexes **Ir1 – Ir5** in argon-sparged CH$_3$CN solution were determined by the relative actinometry method[55] using [Ru(bpy)$_3$]Cl$_2$ (Φ_{em} = 0.097, λ_{ex} = 436 nm)[56] as the standard. The nanosecond transient absorption (TA) spectra and decays, triplet excited-state quantum yields, and triplet lifetimes were collected on argon-sparged (40 min) acetonitrile solutions on an Edinburgh LP920 laser flash photolysis spectrometer using the third harmonic output (355 nm) of a Nd:YAG laser (Quantel Brilliant, pulsewidth ~4.1 ns, repetition rate was set to 1 Hz). Molar

extinction coefficients (ε_{T1-Tn}) for triplet excited states were determined by the singlet depletion method[57] at the TA band maxima, and quantum yields for triplet excited state formation were measured according to the relative actinometry method[58] using the ε_{T1-Tn} values, with SiNc in benzene as the reference ($\varepsilon_{590} = 70{,}000$ $M^{-1}cm^{-1}$, $\Phi_T = 0.20$).[59]

Singlet Oxygen Quantum Yields.

Singlet oxygen quantum yields (Φ) were determined for the PF_6^- salts of the complexes directly from sensitized singlet oxygen emission centered at 1268 nm using a PTI Quantamaster equipped with a Hamamatsu R5509-42 near-infrared PMT. The metal complexes were prepared in spectroscopic-grade CH_3CN at 5 μM, and the measurements were made under ambient oxygen concentration (21%). Φ was calculated relative to the standard $[Ru(bpy)_3](PF_6)_2$ (Φ = 0.56 in aerated CH_3CN)[60] according to Eq 1, where I, A, and η represent integrated emission intensity, absorbance at the excitation wavelength, and refractive index of the solvent, respectively. Values calculated for Φ were reproducible to within <5%.

$$\Phi_\Delta = \Phi_{\Delta s}\left(\frac{I}{A}\right)\left(\frac{A_s}{I_s}\right)\left(\frac{\eta^2}{\eta_s^2}\right) \quad \text{Eq1}$$

DFT Calculations.

Density functional theory (DFT) and time-dependent DFT (TDDFT) calculations on Ir(III) complexes were performed using the Gaussian09 quantum software package.[61] The basis sets used in all calculations were LANL2DZ[62–64] for Ir(III) and 6-31G*[65–69] for other non-metal atoms. Unlike the previous Ir(III) complexes studied,[25,70,71] complexes **Ir1 - Ir5** have two metal centers connected by fluorenylbisterpyridyl ligand, which makes long-range interactions critical for the description of both geometry and excited state properties. Therefore, here we used the long-range corrected hybrid function, ωB97XD, which was designed to capture long-range atom-atom dispersion.[72] Implicit solvent effects were incorporated by the conductor-like polarizable continuous model (CPCM)[73,74] simulating the effects of acetonitrile. The long aliphatic side chains on fluorene were replaced with butyl groups to reduce the computational cost. This reduction does not affect the optical properties of the complexes in the visible spectral region, since octyl groups do not contribute any electronic transitions in this energy range.

The absorption spectra for the Ir(III) complexes were generated by broadening the lowest 100 singlet vertical excitations computed by TDDFT[75,76] using the functional and basis sets described above. To broaden the vertical excitation to generate spectra in terms of molar absorptivity units ($L\cdot mol^{-1}\cdot cm^{-1}$) the method described by Bjorgaard and co-workers was followed.[77] The shape of the spectra generated by broadening the vertical excitation computed by TDDFT quantitatively agreed well, except for about ~0.6 eV blue-shift, which is expected for the ωB97XD functional applied to conjugated systems[78] (see Table S1 of Supporting Information for the energy differences of the experimental and theoretical transitions of the first absorption band). To align the theoretical spectra with the

experimental spectra, all transitions energy were red-shifted by −0.55 eV To characterize the type of excitation for the Ir(III) complexes, natural transition orbitals (NTOs)[79] were generated using Gaussian09 software. NTOs allow for representing an excitation as the electron and hole pair, while preserving the many-body nature of the excited states. Due to the high symmetry of these dinuclear complexes, multiple transition densities that only differ on which metal center electronic density is localized contribute to some excitations. Therefore, only uniquely representative NTOs are shown for those excitations and those states are indicated by "*" in Tables 2 and S2. The visualization of the NTOs were done utilizing Visual Molecular Dynamics (VMD)[80] with isosurface of 0.02.

Photobiological Activity Studies.

The experimental details for cell culture, cytotoxicity and photocytotoxicity studies, confocal microscopy, and DNA mobility-shift assays are the same as those described in our previous published work[24,25] and are presented in the Supporting Information.

RESULTS AND DISCUSSION

Electronic Absorption.

The experimental UV–vis absorption spectra of complexes **Ir1 - Ir5** were recorded in acetonitrile (Figure 1a), and the absorption band maxima and molar extinction coefficients are listed in Table 1. The absorption follows Beer's law in the solutions used in our study (i.e. 5×10^{-6} to 1×10^{-4} mol·L^{-1}), indicating that no ground-state aggregation was formed in the tested concentration range. The strong absorption bands in the range of 250-350 nm and 350-500 nm are predominantly assigned to $^1\pi,\pi$* transitions localized on the terminal tridentate ligands, and the bridging ligand, respectively. These assignments are supported by the NTOs corresponding to the major transitions contributing to these bands (Supporting Information Table S2 and Table 2). Attribution of the absorption bands of 350-500 nm to the bridging ligand localized $^1\pi,\pi$* transition is in line with that revealed in the dinuclear Ir(III) complexes with trisbidentate ligands and diethynylaryl substituted diketopyrrolopyrrole bridging ligand.[81,82] However, NTOs of **Ir1** – **Ir4** in Table 2 show that some charge transfer transitions, *i.e.* ^{1}MLCT, ^{1}LLCT (ligand-to-ligand charge transfer) or ^{1}ILCT (intraligand charge transfer) contributed to the 350-500 nm bands as well. Contributions of the charge transfer configurations to the 350-500 nm absorption bands are partially reflected by the insignificant but noticeable negative solvatochromic effects (Figure S3 in Supporting Information), especially in **Ir2** that has more ^{1}ILCT character (see NTOs in Table 2). In contrast, the charge transfer transitions in **Ir5** became more distinguishable and energetically separated from the bridging ligand localized $^1\pi,\pi$* transition. This is clearly evidenced by the appearance of the new absorption band at 520 nm in **Ir5**.

Comparison of the absorption spectra of **Ir1** and **Ir2** revealed that incorporation of the C≡C bonds to the bridging ligand caused a broadening and a red-shift of the bridging ligand localized $^1\pi,\pi$* absorption band due to the extended π-conjugation. Replacing the terminal terpyridyl ligands in **Ir1** by N^C^N (1,3-dipyridyl-4,6-dimethylbenzene) ligands in **Ir3** induced a blue-shift of the 350-500 nm absorption band and incorporated more terminal ligands based $^1\pi,\pi$* transition and ^{1}LLCT/^{1}MLCT character to this band (see NTOs for **Ir3**

in Table 2); while changing the terminal ligands to C^N^N (4,6-diphenyl-2,2′-bipyridine) ligands in **Ir4** only caused a slight blue-shift of this band with respect to that in **Ir1**. In contrast, when the terminal ligands were changed to C^N^C (2,4,6-triphenylpyridine) ligands in **Ir5**, the transition energies, intensities, and the shape of the low-energy absorption bands changed pronouncedly from those of **Ir1**. This can be attributed to the distinct nature of the lowest energy optical transition in these two complexes. As the NTOs in Table 2 indicated, the stronger σ-donating ability of the phenyl rings on the C^N^C ligand delocalized the hole of the S_1 transition mainly to the 2,6-diphenyl rings and to the metal d orbitals, while the electron was predominantly on the terpyridyl ligands. Thus, the lowest-energy optical transition in **Ir5** is predominantly the ^{1}LLCT/^{1}MLCT transition, which is in contrary to the bridging ligand localized $^1\pi,\pi^*$ transition in **Ir1**. The drastic change of the dominant optical transitions accounts for the different features of the low-energy absorption bands in **Ir5** with respect to that in **Ir1**.

Photoluminescence.

The emission of **Ir1** - **Ir5** was studied in different solvents at room temperature. The observed emission all exhibited large Stokes shifts with respect to the corresponding excitation wavelength, they were all long-lived (several to tens of μs), and sensitive to the presence of oxygen. Thus the emission was attributed to phosphorescence. The normalized emission spectra of **Ir1** - **Ir5** in acetonitrile are displayed in Figure 2, and the spectra in other solvents are given in SI Figure S4. The emission parameters are listed in Table 1 and Table S3 of SI. The emission of **Ir1** and **Ir4** resembled each other, both showing some vibronic structures, with much longer lifetimes and higher emission quantum yields compared to the other three complexes, and exhibiting minor solvatochromic effects. The vibronic spacing between the 580 nm and 620 nm bands is approximately 1150 cm^{-1} and 1090 cm^{-1} in **Ir1** and **Ir4**, respectively, which is in accordance with the aromatic vibrational mode of the terpyridyl ligands. Thus, the emission of these two complexes can be assigned predominantly to the ligand localized $^3\pi,\pi^*$ state. However, the lifetime of **Ir1** is one order of magnitude shorter than that of **Ir4**. This could be attributed to the weaker ligand field of the terpyridyl ligand with respect to that of the C^N^N ligand that contains the stronger σ-donating 6-phenyl ring. The nonradiative metal-centered ^{3}d,d state is thus situated more closely to the low-lying emissive $^3\pi,\pi^*$ state and becomes thermally accessible in **Ir1** compared to that in **Ir4**. This adds an additional decay path for the emitting $^3\pi,\pi^*$ state in **Ir1** and consequently reduces its lifetime. For **Ir2**, **Ir3**, and **Ir5**, the emission spectra are featureless and broader, the lifetimes are less than 2 μs and the emission quantum yields are quite low, and the solvatochromic effect is more pronounced. All these characters imply charge transfer nature of the emitting states in these three complexes. Referring to the NTOs corresponding to the low-energy singlet charge transfer transitions shown in Table 2, it is reasonable to speculate that the emitting state of **Ir2** could be the ^{3}ILCT state and they are the ^{3}LLCT/^{3}MLCT states in **Ir3** and **Ir5**. It appeared that either extending the π-conjugation of the bridging ligand in **Ir2**, or varying the terminal tridentate ligands in **Ir3** and **Ir5** changed the nature of the emitting state from the $^3\pi,\pi^*$ state in **Ir1** to ^{3}CT states. In addition, variation of the terminal tridentate ligands impacted the emission energies in **Ir3** – **Ir5** compared to that in **Ir1**, with a slight blue-shift of the emission in **Ir4** while a salient

red-shift in **Ir3** and **Ir5**. The red-shifted emission in **Ir3** and **Ir5** with respect to that in **Ir1** could possibly be rationalized by the stronger σ-donating ability of the phenyl rings on the terminal tridentate N^C^N and C^N^C ligands, which raised the energies of the terminal ligand and the metal d orbital based holes and thus reduced the energy gaps between the holes and electrons (likely localized on the terpyridyl motifs). Consequently, the ^{3}LLCT/^{3}MLCT emission energies of **Ir3** and **Ir5** are reduced.

Transient Absorption.

To further understand the triplet excited–state characteristics, the nanosecond transient absorption (TA) studies of complexes **Ir1** – **Ir5** were conducted in acetonitrile solutions. The TA spectra of **Ir1** – **Ir5** at zero delay after excitation are presented in Figure 3 and the TA parameters are provided in Table 1. The time-resolved TA spectra of **Ir1** – **Ir5** are provided in Supporting Information Figure S5. The triplet lifetimes deduced from the decay of TA for **Ir1** – **Ir4** are similar to their emission lifetimes in acetonitrile. Therefore, we consider that the observed TA of these complexes was from the excited states that emit. In contrast, **Ir3** exhibited a biexponential decay in its TA signals, with the longer lifetime being consistent with the emission lifetime. This implies that the long-lived TA signal in **Ir3** could from the emitting excited state as well.

The TA spectra of **Ir1** – **Ir5** all possessed very broad positive absorption band(s) from the visible to the near-IR region, *i.e.* 463-800 nm for **Ir1**, 495-800 nm for **Ir2**, 459-800 nm for **Ir3**, 455-800 nm for **Ir4**, and 538-800 nm for **Ir5**. Bleaching occurred in the region corresponding to the low-energy absorption bands. Considering the similar shape of the TA spectra of **Ir1** and **Ir4** to that of our previously reported dinuclear platinum(II) complex with the same bridging ligand,[48] and the similar lifetimes to those of emission, we tentatively attribute the contributing transient absorbing excited state predominantly to the bridging ligand localized $^3\pi,\pi^*$ state. While for **Ir2** and **Ir5**, the transient absorbing states are likely to be the ^{3}CT state(s), *i.e.* predominantly ^{3}ILCT for **Ir2** and ^{3}LLCT/^{3}MLCT states for **Ir5**. In contrast to **Ir1**, **Ir2**, **Ir4** and **Ir5** that exhibited monoexponential decays in their TA signals, the TA signal of **Ir3** followed a biexponential decay. The short-lived transient species had a lifetime of ~30 ns and gave rise to a spectrum reminiscent to those of **Ir1** and **Ir4**; while the long-lived species had a lifetime of ~1.7 μs, which is consistent with the lifetime obtained from the decay of emission, and the TA was much weaker and featureless. In view of the different spectral features at the shorter and longer decay time and the reminiscence of the spectra to those of **Ir1/Ir4** and **Ir2/Ir5**, respectively, we tentatively assign the short-lived species to the high-lying bridging ligand localized $^3\pi,\pi^*$ state; while the long-lived species to the emitting ^{3}LLCT/^{3}MLCT state. The formation of a rapidly decaying higher excited state that subsequently leads to the lower-lying, long-lived emitting state has been reported for a mononuclear Ir(III) complex [(dpb)-Ir(tpy-ph(tBu)$_2$)]$^{2+}$ that bears the same N^C^N ligand.[83]

It is noted that the measured triplet quantum yields of these complexes are not quite high, especially for **Ir2**, **Ir3** and **Ir5**. This could be due to the following reasons: (i) The increased π-conjugation of the ligand would decrease the contribution of the transition metal d orbital to the frontier molecular orbitals of the complexes, which would reduce the spin-orbital

coupling in the complexes and decrease the triplet quantum yield. Such a phenomenon has been reported in many Pt(II) and Ir(III) complexes.[25,70,84] (ii) When a transition-metal complex is excited, especially when high-energy excitation is utilized, population of more than one triplet excited states is possible.[70,85–91] However, not all of the populated triplet excited states contribute to excited-state absorption. In such a case, the calculated triplet quantum yield based on the observed TA signal could be significantly lower than the actual intersystem crossing quantum yield.

Singlet Oxygen Generation.

Production of $^1O_2$ is known to have cytotoxic effects on cells, and thus compounds that generate $^1O_2$ under cell-free conditions might be expected to act as *in vitro* PDT agents. The Ir(III) complexes **Ir1 – Ir5** were assessed for singlet oxygen ($^1O_2$) sensitization in cell-free conditions through direct measurement of $^1O_2$ emission at 1270 nm. [Ru(bpy)$_3$](PF$_6$)$_2$ was used as the standard, with a reported $^1O_2$ quantum yield (Φ) of 0.56 in air-saturated CH$_3$CN.[60] The calculated Φ values for all of the complexes were less than 40%. The efficiencies for $^1O_2$ production ranged from 4% for **Ir3** to 38% for **Ir4**, with **Ir1**, **Ir2** and **Ir5** yielding similar values (22-28%). Despite having some absorption at wavelengths longer than 500 nm, $^1O_2$ yields were maximal with blue excitation. For N^N^N terminal tridentate ligands, the presence of the ethynyl groups for extending π-conjugation did not alter the singlet oxygen quantum yield as **Ir1** and **Ir2** gave very similar values for Φ. When each terminal tridentate ligand of **Ir1** had two of its nitrogens replaced with cyclometalating carbons (C^N^C) as in **Ir5**, the $^1O_2$ yield decreased only slightly. These limited comparisons appear to indicate that substantial structural changes have little to no effect on Φ. However, when only one nitrogen of each terminal tridentate ligand of **Ir1** was replaced by carbon (C^N^N) as in **Ir4**, the $^1O_2$ yield increased to almost 40%. Clearly, there are structural combinations in this family of complexes that do influence Φ. The most dramatic impact on Φ occurred for **Ir3**, where the terminal tridentate ligands were N^C^N with methyl substitution at R$_1$ but no phenyl group at R. In this case, the $^1O_2$ yield decreased by almost tenfold.

It is also worthy of noting that the Φ values for **Ir2**, **Ir4** and **Ir5** are higher than the measured triplet quantum yields (Φ_T, Table 1). This is not very surprising because population of excited states is wavelength dependent, which could result in different decay pathways.[91] In the Φ_T measurement, 355 nm excitation was used; while low-energy excitation (*i.e.* 411 – 468 nm) was used in the Φ measurement. A 355-nm excitation in the TA measurement could populate more than one triplet excited states,[70,85–91] which might not only impact the Φ_T value measurement as discussed in the TA section, but could also reduce the population of the excited state that generates singlet oxygen because of the competing population of the other non-$^1O_2$-generating triplet excited states. In our previous study on the monocationic tris-bidentate Ir(N^N)(C^N)$_2$ complexes, we have demonstrated that the singlet oxygen generation efficiency is wavelength dependent, with lower-energy excitation resulting in higher Φ values in those Ir(III) complexes.[24] We speculate the same case for the complexes studied in this work.

Cytotoxicity and Photocytotoxicity.

To understand whether the photophysical properties of these Ir(III) complexes could lead to photobiological effects, the cytotoxicity profiles of **Ir1 – Ir5** were assessed in SK-MEL-28 malignant melanoma cells under three conditions: (i) dark, (ii) illumination with broadband visible light, and (iii) illumination with red LEDs emitting at 625 nm. Cytotoxic and photocytotoxic activities were quantified as the effective concentration required to reduce the cell viability to 50% (EC_{50}) under a given condition. Briefly, cells growing in log phase were dosed with nine concentrations of the complex between 1 nM and 300 μM, incubated for 16 h, and were then subjected to a sham (dark) or light treatment. The light treatments were delivered at a fluence of 100 J·cm^{-2} with an irradiance of 35.7 mW·cm^{-2} or 32.3 mW·cm^{-2} for visible and red light, respectively. After a 48 h incubation period, cell viability was quantified based on the ability of viable cells to reduce resazurin to resorufin. EC_{50} values were determined from sigmoidal fits of the dose-response curves (Figure 4, Table 3). The phototherapeutic index (PI), a measure of the therapeutic margin for *in vitro* PDT, was calculated as the ratio of dark to light EC_{50} values and determined for each complex and irradiation condition. The dark toxicities of **Ir1 – Ir5** toward normal human skin fibroblasts (CCD-1064Sk) were also measured to determine any selectivity for cancer cells over normal cells. The ratio of the dark CCD-1064Sk EC_{50} value for a given complex and its dark SK-MEL-28 EC_{50} value yielded the selectivity factor (SF), where SF > 1 indicates selectivity toward the cancerous cell line. Selective activity toward the cancer cell line is not a requirement for the PDT agent as long as the dark toxicity of the photosensitizer is low and the PI is relatively large. Rather, the spatiotemporal control of the light treatment provides the selectivity known for PDT. Nevertheless, for *in vivo* applications, selective activity toward cancer cells over normal, healthy cells is an added benefit.

The dark cytotoxicities of complexes **Ir1 – Ir5** toward SK-MEL-28 melanoma cells ranged from 16.9 to 82.6 μM, with **Ir1** being the least cytotoxic in the absence of a light trigger and **Ir2** and **Ir4** being the most cytotoxic (Table 3 and Figures 4–5). With the exception of **Ir3** (SF = 1), the other dinuclear Ir(III) complexes exhibited some selective cytotoxicity toward the melanoma cancer cells relative to the normal human skin fibroblast cells. SF values followed the order **Ir5** > **Ir2** ≈ **Ir4** > **Ir1** > **Ir3**, with **Ir5** exhibiting two-fold greater dark toxicity toward SK-MEL-28 cells and **Ir3** showing no selectivity. The selective cytotoxicity observed for **Ir2** and **Ir4** was almost as great as that for **Ir5** (SF = 1.9 versus SF = 2.0). **Ir1** and **Ir5** had dark EC_{50} values greater than 100 μM in the CCD-1064Sk cell line, and were thus considered to be completely nontoxic to the normal skin fibroblasts. In both cell lines, the dark toxicity was greatest for **Ir2** and **Ir4** and least for **Ir1** and **Ir5**.

All of the complexes in the series could be activated with visible light to become powerful phototoxins, with EC_{50} values ranging from 170 nM to 1 μM and PIs ranging from 20 to 288. **Ir3** and **Ir4** were the most phototoxic at 170 nM, while **Ir1**, **Ir2**, and **Ir5** were similar (visible EC_{50} = 0.75–1.0 μM). Photoactivation of the complexes with red light (625 nm) did not enhance the cytotoxicity over what was observed in the dark treatment, yielding PIs close to 1.0 in all cases. The photobiological activities of **Ir1** - **Ir5** were tested with red light, despite their very low molar extinction coefficients in this region, because other metal

complex systems with π-expansive ligands have been shown to yield potent *in vitro* red PDT effects even with molar extinction coefficients less than 100 $M^{-1} \cdot cm^{-1}$.[20]

The presence of visible PDT effects (presumably due to the shorter wavelengths) but lack of red PDT effects suggests that direct population of the highly photosensitizing triplet states is not efficient in this class of complexes and that access to these states must be gained through [1]MLCT states. The photocytotoxicity profiles in SK-MEL-28 under two irradiation conditions along with the dark cytotoxicity profiles in two cell lines are summarized in the activity plot in Figure 5.

The visible PDT effect followed the order **Ir3** > **Ir1** > **Ir4** > **Ir5** > **Ir2**, with **Ir3** being the most promising photosensitizer based on its PI of 288 and nanomolar photocytotoxicity. **Ir1** and **Ir4** both had PIs greater than 100, but the dark toxicity associated with **Ir4** in both cell lines limits its potential for *in vivo* applications. The source of the PDT effect for this series has not been established. The $^1O_2$ quantum yields measured under cell-free conditions followed the order **Ir4** > **Ir1** > **Ir2** > **Ir5** > **Ir3**, with **Ir1** and **Ir2** being very similar. **Ir3** was the poorest $^1O_2$ generator, yet it was one of the most phototoxic complexes of the series. On the other hand, **Ir4** was the best sensitizer of $^1O_2$ and was as phototoxic as **Ir3**. Therefore, $^1O_2$ may play a role in the PDT mechanism for some complexes but not others in this series, or the intracellular $^1O_2$ quantum yields may differ from those measured under cell-free conditions. Regardless, certain members of this new series of dinuclear Ir(III) complexes have been identified as promising PDT agents for further investigation.

While the structural diversity in such a small library is somewhat limited, it was possible to identify some trends regarding structural features that affect cytotoxicity. For example, incorporation of ethynyl linkers as in **Ir2** turned the relatively nontoxic complex **Ir1** into one of the most potent dark cytotoxic complexes of the series (Table 3). Likewise, replacement of the terminal tridentate N^N^N ligands of **Ir1** with C^N^N as in **Ir4** increased the dark cytotoxicity substantially, while replacement with C^N^C as in **Ir5** had only a very minor effect that differed between the two cell lines. In SK-MEL-28, the dark toxicity increased slightly, and in CCD-106Sk, the dark toxicity decreased slightly. The complex that departed the most structurally from the other complexes in the series and was identified as being the most promising PDT lead, **Ir3**, was intermediate in terms of dark cytotoxicity ($EC_{50} \approx 50$ μM) with almost no difference between the two cell lines.

In terms of structural features affecting photocytotoxicity, the nature of the terminal tridentate ligand played some role as **Ir4** (C^N^N) was more than six fold more phototoxic than **Ir5** (C^N^C). While the presence of an ethynyl linker increased the dark cytotoxicity substantially in both cell lines, its presence did not impact the photocytotoxicity toward SK-MEL-28 in any significant way. The differences in dark and light-triggered cytotoxicity toward SK-MEL-28 cells alongside differences in dark cytotoxicity between normal and cancerous cells for certain members of this series indicate that even minor structural modifications can have a major impact on biological activity.

Cellular Imaging.

The phosphorescence from complexes **Ir1** – **Ir5** was used to probe cellular uptake by SK-MEL-28 melanoma cells with or without a light treatment (Figure 6). The excitation from a 458/488 nm argon-krypton laser matched the excitation maxima of the complexes and was used in conjunction with a 475-nm long pass filter to collect the emission from the complexes. The images were collected after a brief 1-h incubation period to ensure that some viable cells remained. Light-treated cells were illuminated with a broadband visible light (50 J·cm^{-2}) that was 50% of the fluence used in the cellular assays in order to capture a fraction of viable cells.

Untreated SK-MEL-28 cells have a dendritic morphology. Treatment with the dinuclear Ir(III) complexes with or without illumination caused a conversion from dendritic to spherical morphology. The complexes showed detectable phosphorescence when associated with or in dead/dying and compromised cells with or without a light treatment. Only **Ir1** appeared to be readily taken up into SK-MEL-28 cells in the dark at the observation time point. However, phosphorescence from the Ir(III) complexes in all cells was apparent after a light treatment, suggesting photoactivated uptake. For light-treated cells incubated with **Ir1**, it was not possible to discern subcellular localization because only cellular debris was present at the observation time point. However, **Ir2** and **Ir4** localized to the cytoplasm and multiple nucleoli whereas **Ir3** and **Ir5** were distributed throughout the cell and phosphoresced with a very intense signal by comparison.

Qualitatively, SK-MEL-28 cells treated with **Ir4** with or without visible illumination appeared the most viable with healthy morphology in the imaging experiments but were the most susceptible in the cellular assays, highlighting the need to exercise caution when reconciling the cellular assay results with confocal imaging performed at different time points post-complex-delivery and post-irradiation and a different light fluence. When the conditions were similar, the imaging experiments did reflect the trends observed in the cellular assays with SK-MEL-28 but did not provide any information regarding uptake and localization since all cells were dead/dying but at slightly different stages. A quantitative comparison of the cellular uptake and induced morphological changes for the five complexes and correlations to cellular cytotoxicity or photocytotoxicity were not attempted given the need to alter incubation and illumination times to preserve some viable cells. Rather, the purpose of the imaging was to highlight the potential of these new Ir(III) complexes as theranostic agents based on their abilities to yield visible PDT effects and to be simultaneously imaged by their inherent phosphorescence.

DNA Interactions.

The ability of the Ir(III) complexes to act as DNA photocleaving agents was investigated to establish whether light-mediated DNA damage could contribute to the observed *in vitro* PDT effects for this class of photosensitizers. Supercoiled plasmid DNA (20 μM bases) was treated with increasing concentrations of **Ir1** – **Ir5** and then exposed to a visible light treatment of 14 J·cm^{-2} (Figure 7, lanes 3–14). The fluence is less that what was used in the cellular assays because the DNA is more susceptible to damage by the light treatment alone when not protected by the cellular environment. The photolyzed samples were then

electrophoresed and compared to DNA alone with or without a light treatment (Figure 7, lanes 1 and 2) and DNA exposed to the highest concentration of the complex without a light treatment (Figure 7, lane 15). The gels were cast either with the DNA stain ethidium bromide (EB) incorporated or without EB and stained after electrophoresis (non-EB). EB gels allow detection of photocleavage not compounded by DNA unwinding; the non-EB gels allow detection of DNA unwinding in addition to photocleavage. Under the conditions employed for this gel electrophoretic mobility shift assay, undamaged supercoiled DNA (Form I) migrates the farthest in the gel, while aggregated/condensed DNA (Form IV) migrates very little from the loading well. Plasmid DNA that has undergone single-strand breaks (Form II) will relax and migrate between Forms I and IV, and plasmid DNA with frank double-strand breaks or double-strand breaks that arise from the build-up of single-strand breaks on opposing strands within about 16 base pairs (Form III) will migrate slightly faster than Form II. Forms I, II, and IV were detectable in both EB and non-EB gels. None of the complexes acted as DNA unwinders on the non-EB gel, indicating that they most likely do not act as DNA intercalators.

All of the complexes showed some ability to photocleave DNA (Figure 7) in a cell-free environment. Qualitatively, DNA photocleaving ability appeared to increase in the order **Ir5** < **Ir2** ≈ **Ir3** < **Ir4** < **Ir1**. The formation of Form IV DNA and the disappearance of gel bands precluded a more quantitative comparison, but some general trends could still be discerned.

Despite its $^1O_2$ quantum yield of 22%, **Ir5** appeared to show the weakest interactions with DNA (although some strand breaks to yield detectable Form II[92] were observed toward the highest concentrations). On the other hand, **Ir1**, with a similar Φ, acted as a much more potent DNA photocleaving agent, converting a significant amount of supercoiled Form I DNA to Form II DNA at a metal complex (MC) concentration of only 1 μM and 20 μM DNA bases (Figure 7a, lane 4). At similarly low [MC]:[bases] ratios of 0.05, **Ir2** – **Ir5** caused no detectable strand breaks, which can be seen by comparing lane 4 for all of the complexes. **Ir4**, with the largest value for Φ, photocleaved DNA in a concentration-dependent manner to yield Form II DNA as expected.

All of the complexes caused DNA aggregation/condensation, although **Ir5** produced trace amounts of Form IV DNA only at the highest complex concentrations investigated. Interestingly, **Ir5** was the only complex that did not cause the DNA gel bands to disappear. The lack of DNA staining by EB for the other complexes could be due to fluorescence quenching of the EB dye by the complex, their competition for EB intercalation sites, or their distortion of the DNA helix that prevents EB binding.

Clearly, the structural differences between the Ir(III) complexes of this small library resulted in markedly different interactions with DNA, and possibly different photophysical interactions with the EB dye. The observation that **Ir5** shows marginal DNA interactions in the gel electrophoretic analysis yet acts as an *in vitro* PDT agent suggests that DNA may not be the intracellular target, at least for this particular complex. In fact, DNA photodamage did not correlate clearly with $^1O_2$ quantum yields across the series, which also supports the notion that another biological target is likely involved. However, the cell-free experiment does not accurately mimic the complexity of the cellular environment and dynamic

processes (e.g., uptake, efflux, metabolism, and localization), and *in vitro* DNA damage and $^1O_2$ damage cannot be ruled out completely. What can be gleaned from the DNA photocleavage study is that minor structural changes in this series have profound effects on the complex interactions with biological macromolecules such as DNA, which is in agreement with their different profiles in the cellular assays and imaging studies.

CONCLUSIONS

The synthesis, photophysical and photobiological properties of a family of water-soluble cationic dinuclear iridium(III) complexes (**Ir1** - **Ir5**) were explored. The influence of the bridging and terminal ligands on the photophysical properties of the complexes was investigated. Compared to **Ir1** that had the single bond connection between the fluorenyl motif and the terpyridyl ligands on the bridging ligand, the extended π-conjugation afforded by the ethynyl connectors of the bridging ligand in **Ir2** red-shifted the UV-vis absorption markedly, but the low-lying ^{3}CT state of **Ir2** accelerated nonradiative decay and resulted in weak phosphorescence. A considerable bathochromic shift also occurred in the absorption and emission of **Ir5**, owing to the stronger σ-donating ability of the negatively charged coordinating carbon relative to nitrogen and thus more charge transfer from the C^N^C ligands to the terpyridyl ligands. Complexes **Ir1 – Ir5** all featured with broad positive absorption bands spanning the visible region and NIR regions in their nanosecond TA spectra. However, the triplet state TA lifetimes of **Ir1** and **Ir4** were much longer (3.1 μs and 48 μs, respectively) than those of **Ir2**, **Ir3** and **Ir5**, implying the dominant bridging ligand-localized $^3\pi,\pi^*$ nature for the lowest triplet states in **Ir1** and **Ir4** rather than the ^{3}CT states for the other three complexes. Based on photophysical properties alone, **Ir4** was predicted to be the best *in vitro* PDT agent.

All of the Ir(III) complexes of this study exhibited photobiological effects when activated with visible light, but were inactive with single-wavelength red light (625 nm). Thus, the *in vitro* PDT effects with broadband visible light were attributed to the shorter wavelengths. Some of the complexes showed selective cytotoxicity toward cancerous human melanoma cells over normal human skin fibroblasts. The photobiological trends could not be readily correlated to any differences in photophysical properties despite accessible long-lived $^3\pi,\pi^*$ states often resulting in red PDT activity. But the long-lived **Ir4** did not yield a red PDT effect, nor did any of the other complexes due to the lack of ground-state absorption in the red. Rather, **Ir3** emerged as a promising photosensitizer for further investigation owing to its nanomolar photocytotoxicity and visible PI > 280, with **Ir1** and **Ir5** also having suitable profiles. This small library of just five complexes proved to be a rich source of photophysical and photobiological diversity with only minor structural modifications. They gave $^1O_2$ quantum yields that ranged from 4 to 38%, light EC_{50} values from nanomolar to micromolar, dark toxicities that ranged from 32 to >140 μM, and DNA interactions that were characteristic for a particular cationic complex. For *in vitro* PDT applications in particular, there was a clear indication that the terminal tridentate N^C^N ligand performed best when combined with methyl substituents on the central cyclometalating ring and no ethynyl linkers between terminal ligands and the central fluorene unit. Thus, **Ir3** will serve as the lead complex for future studies and as the parent complex of a second-generation library.

Supplementary Material

Refer to Web version on PubMed Central for supplementary material.

REFERENCES

(1). Storr T; Thompson KH; Orvig C Design of Targeting Ligands in Medicinal Inorganic Chemistry. Chem. Soc. Rev 2006, 35, 534–544. [PubMed: 16729147]

(2). Dasari S; Tchounwou PB Cisplatin in Cancer Therapy: Molecular Mechanisms of Action. Eur. J. Pharmacol 2014, 740, 364–378. [PubMed: 25058905]

(3). Bergamo A; Gaiddon C; Schellens JHM; Beijnen JH; Sava G Approaching Tumour Therapy beyond Platinum Drugs: Status of the Art and Perspectives of Ruthenium Drug Candidates. J. Inorg. Biochem 2012, 106, 90–99. [PubMed: 22112845]

(4). Dabrowiak JC Anticancer Agents Beyond Cisplatin In Metals in Medicine; John Wiley & Sons, Ltd, 2017; pp 157–216.

(5). Trondl R; Heffeter P; Kowol CR; Jakupec MA; Berger W; Keppler BK NKP-1339, the First Ruthenium-Based Anticancer Drug on the Edge to Clinical Application. Chem. Sci 2014, 5, 2925–2932.

(6). Schoenhacker-Alte B; Mohr T; Pirker C; Kryeziu K; Kuhn P-S; Buck A; Hofmann T; Gerner C; Hermann G; Koellensperger G; et al. Sensitivity towards the GRP78 Inhibitor KP1339/IT-139 Is Characterized by Apoptosis Induction via Caspase 8 upon Disruption of ER Homeostasis. Cancer Lett. 2017, 404, 79–88. [PubMed: 28716523]

(7). Burris HA; Bakewell S; Bendell JC; Infante J; Jones SF; Spigel DR; Weiss GJ; Ramanathan RK; Ogden A; Von Hoff D Safety and Activity of IT-139, a Ruthenium-Based Compound, in Patients with Advanced Solid Tumours: A First-in-Human, Open-Label, Dose-Escalation Phase I Study with Expansion Cohort. ESMO Open 2017, 1, e000154. [PubMed: 28848672]

(8). Mari C; Gasser G Lightening up Ruthenium Complexes to Fight Cancer? Chim. Int. J. Chem 2015, 69, 176–181.

(9). Mari C; Pierroz V; Ferrari S; Gasser G Combination of Ru(II) Complexes and Light: New Frontiers in Cancer Therapy. Chem. Sci 2015, 6, 2660–2686. [PubMed: 29308166]

(10). Knoll JD; Turro C Control and Utilization of Ruthenium and Rhodium Metal Complex Excited States for Photoactivated Cancer Therapy. Coord. Chem. Rev 2015, 282–283, 110–126.

(11). Poynton FE; Bright SA; Blasco S; Williams DC; Kelly JM; Gunnlaugsson T The Development of Ruthenium(II) Polypyridyl Complexes and Conjugates for in Vitro Cellular and in Vivo Applications. Chem. Soc. Rev 2017, 46, 7706–7756. [PubMed: 29177281]

(12). Bonnett R Chemical Aspects of Photodynamic Therapy; Gordon and Breach Science Publishers, 2000.

(13). van Straten D; Mashayekhi V; de Bruijn H; Oliveira S; Robinson D Oncologic Photodynamic Therapy: Basic Principles, Current Clinical Status and Future Directions. Cancers 2017, 9, 19.

(14). Hamblin MR; Huang Y-Y Handbook of Photomedicine; Taylor & Francis, 2014.

(15). Abrahamse H; Hamblin MR New Photosensitizers for Photodynamic Therapy. Biochem. J 2016, 473, 347–364. [PubMed: 26862179]

(16). Shi G; Monro S; Hennigar R; Colpitts J; Fong J; Kasimova K; Yin H; DeCoste R; Spencer C; Chamberlain L; et al. Ru(II) Dyads Derived from Alpha-Oligothiophenes: A New Class of Potent and Versatile Photosensitizers for PDT. Coord. Chem. Rev 2015, 282–283, 127–138.

(17). Kaspler P; Lazic S; Forward S; Arenas Y; Mandel A; Lilge L A Ruthenium(II) Based Photosensitizer and Transferrin Complexes Enhance Photo-Physical Properties, Cell Uptake, and Photodynamic Therapy Safety and Efficacy. Photochem. Photobiol. Sci 2016, 15, 481–495. [PubMed: 26947517]

(18). Ford WE; Rodgers MAJ Reversible Triplet-Triplet Energy Transfer within a Covalently Linked Bichromophoric Molecule. J. Phys. Chem 1992, 96, 2917–2920.

(19). McClenaghan ND; Leydet Y; Maubert B; Indelli MT; Campagna S Excited-State Equilibration: A Process Leading to Long-Lived Metal-to-Ligand Charge Transfer Luminescence in Supramolecular Systems. Coord. Chem. Rev 2005, 249, 1336–1350.

(20). Yin H; Stephenson M; Gibson J; Sampson E; Shi G; Sainuddin T; Monro S; McFarland SA In Vitro Multiwavelength PDT with ^{3}IL States: Teaching Old Molecules New Tricks. Inorg. Chem 2014, 53, 4548–4559. [PubMed: 24725142]

(21). Lincoln R; Kohler L; Monro S; Yin H; Stephenson M; Zong R; Chouai A; Dorsey C; Hennigar R; Thummel RP; et al. Exploitation of Long-Lived 3IL Excited States for Metal-Organic Photodynamic Therapy: Verification in a Metastatic Melanoma Model. J. Am. Chem. Soc 2013, 135, 17161–17175. [PubMed: 24127659]

(22). Stephenson M; Reichardt C; Pinto M; Wachtler M; Sainuddin T; Shi G; Yin H; Monro S; Sampson E; Dietzek B; et al. Ru(II) Dyads Derived from 2-(1-Pyrenyl)-1H-Imidazo[4,5-f] [1,10]Phenanthroline: Versatile Photosensitizers for Photodynamic Applications. J. Phys. Chem. A 2014, 118, 10507–10521. [PubMed: 24927113]

(23). Arenas Y; Monro S; Shi G; Mandel A; McFarland S; Lilge L Photodynamic Inactivation of Staphylococcus Aureus and Methicillin-Resistant Staphylococcus Aureus with Ru(II)-Based Type I/Type II Photosensitizers. Photodiag. Photodyn. Ther 2013, 10, 615–625.

(24). Wang L; Yin H; Cui P; Hetu M; Wang C; Monro S; Schaller RD; Cameron CG; Liu B; Kilina S; et al. Near-Infrared-Emitting Heteroleptic Cationic Iridium Complexes Derived from 2,3-Diphenylbenzo[g]Quinoxaline as in Vitro Theranostic Photodynamic Therapy Agents. Dalton Trans. 2017, 46, 8091–8103. [PubMed: 28604869]

(25). Wang C; Lystrom L; Yin H; Hetu M; Kilina S; McFarland SA; Sun W Increasing the Triplet Lifetime and Extending the Ground-State Absorption of Biscyclometalated Ir(III) Complexes for Reverse Saturable Absorption and Photodynamic Therapy Applications. Dalton Trans. 2016, 45, 16366–16378. [PubMed: 27711764]

(26). Majumdar P; Yuan X; Li S; Guennic BL; Ma J; Zhang C; Jacquemin D; Zhao J Cyclometalated Ir(III) Complexes with Styryl-BODIPY Ligands Showing near IR Absorption/Emission: Preparation, Study of Photophysical Properties and Application as Photodynamic/Luminescence Imaging Materials. J. Mater. Chem. B 2014, 2, 2838–2854.

(27). Ye R-R; Tan C-P; He L; Chen M-H; Ji L-N; Mao Z-W Cyclometalated Ir(III) Complexes as Targeted Theranostic Anticancer Therapeutics: Combining HDAC Inhibition with Photodynamic Therapy. Chem. Commun 2014, 50, 10945–10948.

(28). He L; Li Y; Tan C-P; Ye R-R; Chen M-H; Cao J-J; Ji L-N; Mao Z-W Cyclometalated Iridium(III) Complexes as Lysosome-Targeted Photodynamic Anticancer and Real-Time Tracking Agents. Chem. Sci 2015, 6, 5409–5418. [PubMed: 29861886]

(29). Kando A; Hisamatsu Y; Ohwada H; Itoh T; Moromizato S; Kohno M; Aoki S Photochemical Properties of Red-Emitting Tris(Cyclometalated) Iridium(III) Complexes Having Basic and Nitro Groups and Application to pH Sensing and Photoinduced Cell Death. Inorg. Chem 2015, 54, 5342–5357. [PubMed: 25978770]

(30). Jiang X; Zhu N; Zhao D; Ma Y New Cyclometalated Transition-Metal Based Photosensitizers for Singlet Oxygen Generation and Photodynamic Therapy. Sci. China Chem. 2016, 59, 40–52.

(31). Zheng Y; He L; Zhang D-Y; Tan C-P; Ji L-N; Mao Z-W Mix-ligand Iridium(III) Complexes as Photodynamic Anticancer Agents. Dalton Trans. 2017, 46, 11395–11407. [PubMed: 28813052]

(32). Liu J; Jin C; Yuan B; Chen Y; Liu X; Ji L; Chao H Enhanced Cancer Therapy by the Marriage of Metaabolic Alternation and Mitochondrial-targeted Photodynamic Therapy Using Cyclometalated Ir(III) Complexes. Chem. Commun 2017, 53, 9878–9881.

(33). Xiang H; Chen H; Tham HP; Phua SZF; Liu J-G; Zhao Y Cyclometalated Iridium(III)-Complex-Based Mocelles for Glutathione-REsponsive Targeted Chemtherapy and Photodynamic Therapy. ACS Appl. Mater. Interfaces 2017, 9, 27553–27562. [PubMed: 28749655]

(34). Zhang P; Chiu CKC; Huang H; Lam YPY; Habtemariam A; Malcomson T; Paterson MJ; Clarkson GJ; O'Connor PB; Chao H; Sadler PJ Organoiridium Photosensitizers Induce Specific Oxidative Attack on Proteins within Cancer Cells. Angew. Chem. Int. Ed 2017, 56, 14898–14902.

(35). Lv W; Zhang Z; Zhang KY; Yang H; Liu S; Xu A; Guo S; Zhao Q; Huang W A Mitochondria-Targeted Photosensitizer Showing Improved Photodynamic Therapy Effects Under Hypoxia. Angew. Chem. Int. Ed 2016, 55, 9947–9951.

(36). Qiu K; Ouyang M; Liu Y; Huang H; Liu C; Chen Y; Ji L; Chao H Two-photon Photodynamic Ablation of Tumor Cells by Mitochonfria-Targeted Iridium(III) Complexes in Aggregated States. J. Mater. Chem. B 2017, 5, 5488–5498.

(37). Ouyang M; Zeng L; Qiu K; Chen Y; Li L; Chao H Cyclometalated Ir^{III} Complexes as Mitochondria-Targeted Photodynamic Anticancer Agents. Eur. J. Inorg. Chem 2017, 1764–1771.

(38). Xue F; Lu Y; Zhou Z; Shi M; Yan Y; Yang H; Yang S Two in One: Luminescence Imaging and 730 nm Continuous Wave Laser Driven Photodynamic Therapy of Iridium Complexes. Organometallics 2015, 34, 73–77.

(39). Maggioni D; Galli M; D'Alfonso L; Inverso D; Dozzi MV; sironi L; Iannacone M; Collin M; Ferruti P; Ranucci E; D'Alfonso G A Luminescent Poly(amidoamine)-Iridium Complex as a New Singlet-Oxygen Sensitizer for Photodynamic Therapy. Inorg. Chem 2015, 54, 544–553. [PubMed: 25554822]

(40). Nam JS; Kang M-G; Kang J; Park S-Y; Lee SJC; Kim H-T; Seo JK; Kwon O-H; Lim MH; Rhee H-W; Kwon T-H Endoplasmic Reticulum-Localized Iridium(III) Complexes as Efficient Photodynamic Therapy Agents via Protein Modifications. J. Am. Chem. Soc 2016, 138, 10968–10977. [PubMed: 27494510]

(41). Li Y; Lu X-R; Li M-F; Ji L-N; Mao Z-W Cyclometalated Iridium(III) N-Heterocyclic Carbene Complexes as Potnetial Mitochondria Anticancer and Photodynamic Agents. Dalton Trans. 2017, 46, 11363–11371. [PubMed: 28812748]

(42). Tabrizi L; Chiniforoshan H New Cyclometalated Ir(III) Complexes with NCN Pincer and meso-Phenylcyanamide BODIPY Ligands as Efficient Photodynamic Therapy Agents. RSC Adv. 2017, 7, 34160–34169.

(43). McKenzie LK; Sazanovich IV; Baggaley E; Bonnneau M; Guerchais V; Williams JAG; Weinstein JA; Bryant HE Metal Complexes for Two-Photon Photodynamic Therapy: A Cyclometalated Iridium Complex Induces Two-Photon Photosensitization of Cancer under Near-IR Light. Chem. Eur. J 2017, 23, 234–238. [PubMed: 27740703]

(44). Tian X; Zhu Y; Zhang M; Luo L; Wu J; Zhou H; Guan L; Battaglia G; Tian Y Localization Matters: A Nuclear Targeting Two-Photon Absorption Iridium Complex in Photodynamic Therapy. Chem. Commun 2017, 53, 3303–3306.

(45). Cui Y; Wen LL; Shan GG; Sun HZ; Mao HT; Zhang M; Su ZM Di-/Trinuclear Cationic Ir(III) Complexes: Design, Synthesis and Application for Highly Sensitive and Selective Detection of TNP in Aqueous Solution. Sens. Actuators B. 2017, 244, 314–322.

(46). Constable EC 2,2′:6′,2″-Terpyridines: From Chemical Obscurity to Common Supramolecular Motifs. Chem. Soc. Rev 2007, 36, 246–253. [PubMed: 17264927]

(47). Hofmeier H; Schubert US Recent Developments in the Supramolecular Chemistry of Terpyridine-Metal Complexes. Chem. Soc. Rev 2004, 33, 373–399. [PubMed: 15280970]

(48). Ji Z; Li S; Li Y; Sun W Back-to-Back Dinuclear Platinum Terpyridyl Complexes: Synthesis and Photophysical Studies. Inorg. Chem 2010, 49, 1337–1346. [PubMed: 20092284]

(49). Tu S; Li T; Shi F; Wang Q; Zhang J; Xu J; Zhu X; Zhang X; Zhu S; Shi D Convenient One-Pot Synthesis of 4′-Aryl-2,2′:6′,2″-terpyridines and 2,4,6-Triarylpyridines under Microwave Irradiation. Synthesis 2005, 18, 3045–3050.

(50). Wilkinson AJ; Puschmann H; Howard JAK; Foster CE; Williams JAG Luminescent Complexes of Iridium (III) Containing N^C^N-coordinating Terdentate Ligands. Inorg. Chem 2006, 45, 8685–8699. [PubMed: 17029380]

(51). Basnet A; Thapa P; Karki R; Na Y; Jahng Y; Jeong BS; Jeong TC; Lee CS; Lee ES 2,4,6-Trisubstituted Pyridines: Synthesis, Topoisomerase I and II Inhibitory Activity, Cytotoxicity, and Structure–Activity Relationship. Bioorg. Med. Chem 2007, 15, 4351–4359. [PubMed: 17493824]

(52). Adib M; Ayashi N; Mirzaei P An Efficient Synthesis of 2,4,6-Triarylpyridines by Use of Benzyl Halides under Neat Conditions. Synlett 2016, 27, 417–421.

(53). Chirdon DN; Transue WJ; Kagalwala HN; Kaur A; Maurer AB; Pintauer T; Bernhard S [Ir(N^N^N)(C^N)L]⁺: A New Family of Luminophores Combining Tunability and Enhanced Photostability. Inorg. Chem 2014, 53, 1487–1499. [PubMed: 24437359]

(54). Choi D; Kim T; Reddy SM; Kang J Synthesis and Electronic Properties of Double Pincer-type Cyclometalated Iridium Complexes. Inorg. Chem. Commun 2009, 12, 41–44.

(55). Demas JN; Crosby GA The Measurement of Photoluminescence Quantum Yields. A Review.. J. Phys. Chem 1971, 75, 991–1024.

(56). van Houten J; Watts RJ Temperature Dependence of the Photophysical and Photochemical Properties of the Tris(2,2′-bipyridyl) Ruthenium(II) Ion in Aqueous Solution. J. Am. Chem. Soc 1976, 98, 4853–4858.

(57). Carmichael I; Hug GL Triplet-triplet Absorption Spectra of Organic Molecules in Condensed Phases. J. Phys. Chem. Ref. Data 1986, 15, 1–250.

(58). Kumar CV; Qin L; Das PK Aromatic Thioketone Triplets and Their Quenching Behaviour towards Oxygen and Di-t-butylnitroxy Radical. A Laser-Flash-Photolysis Study. J. Chem. Soc., Faraday Trans. 2 1984, 80, 783–793.

(59). Firey PA; Ford WE; Sounik JR; Kenney ME; Rodgers MAJ Silicon Naphthalocyanine Triplet State and Oxygen. A Reversible Energy-transfer Reaction. J. Am. Chem. Soc 1988, 110, 7626–7630.

(60). DeRosa MC; Crutchley RJ Photosensitized Singlet Oxygen and Its Applications. Coord. Chem. Rev 2002, 233–234, 351–371.

(61). Frisch MJ; Trucks GW; Schlegel HB; Scuseria GE; Robb MA; Cheeseman JR; Scalmani G; Barone V; Mennucci B; Petersson GA; et al. Gaussian 09, Revision D.01, Gaussian. Inc., Wallingford, CT, 2013.

(62). Hay PJ; Wadt WR Ab Initio Effective Core Potentials for Molecular Calculations. Potentials for K to Au Including the Outermost Core Orbitals. J. Chem. Phys 1985, 82, 299–310.

(63). Hay PJ; Wadt WR Ab Initio Effective Core Potentials for Molecular Calculations. Potentials for the Transition Metal Atoms Sc to Hg. J. Chem. Phys 1985, 82, 270–283.

(64). Wadt WR; Hay PJ Ab Initio Effective Core Potentials for Molecular Calculations. Potentials for Main Group Elements Na to Bi. J. Chem. Phys 1985, 82, 284–298.

(65). Clark T; Chandrasekhar J; Spitznagel GW; Schleyer PVR Efficient Diffuse Function-Augmented Basis Sets for Anion Calculations. III. The 3-21+G Basis Set for First-Row Elements, Li-F. J. Comput. Chem 1983, 4, 294–301.

(66). Francl MM; Pietro WJ; Hehre WJ; Binkley JS; Gordon MS; DeFrees DJ; Pople JA Self-Consistent Molecular Orbital Methods. XXIII. A Polarization-Type Basis Set for Second-Row Elements. J. Chem. Phys 1982, 77, 3654–3665.

(67). Gill PM; Johnson BG; Pople JA; Frisch MJ The Performance of the Becke-Lee-Yang-Parr (B-LYP) Density Functional Theory with Various Basis Sets. Chem. Phys. Lett 1992, 197, 499–505.

(68). Hariharan PC; Pople JA The Influence of Polarization Functions on Molecular Orbital Hydrogenation Energies. Theor. Chim. Acta 1973, 28, 213–222.

(69). Krishnan R; Binkley JS; Seeger R; Pople JA Self-Consistent Molecular Orbital Methods. XX. A Basis Set for Correlated Wave Functions. J. Chem. Phys 1980, 72, 650–654.

(70). Liu B; Lystrom L; Kilina S; Sun W Tuning the Ground State and Excited State Properties of Monocationic Iridium (III) Complexes by Varying the Site of Benzannulation on Diimine Ligand. Inorg. Chem 2017, 56, 5361–5370. [PubMed: 28398733]

(71). Zhu X; Lystrom L; Kilina S; Sun W Tuning the Photophysics and Reverse Saturable Absorption of Heteroleptic Cationic Iridium (III) Complexes via Substituents on the 6,6′-Bis (Fluoren-2-yl)-2,2′-biquinoline Ligand. Inorg. Chem 2016, 55, 11908–11919. [PubMed: 27934300]

(72). Chai J-D; Head-Gordon M Long-Range Corrected Hybrid Density Functionals with Damped Atom-Atom Dispersion Corrections. PCCP 2008, 10, 6615–6620. [PubMed: 18989472]

(73). Barone V; Cossi M; Tomasi J Geometry Optimization of Molecular Structures in Solution by the Polarizable Continuum Model. J. Comput. Chem 1998, 19, 404–417.

(74). Cossi M; Rega N; Scalmani G; Barone V Energies, Structures, and Electronic Properties of Molecules in Solution with the C-PCM Solvation Model. J. Comput. Chem 2003, 24, 669–681. [PubMed: 12666158]

(75). Marques MA; Gross EK Time-Dependent Density Functional Theory. Annu. Rev. Phys. Chem 2004, 55, 427–455. [PubMed: 15117259]

(76). Ullrich CA Time-Dependent Density-Functional Theory: Concepts and Applications. OUP Oxford: 2011.

(77). Bjorgaard JA; Sifain AE; Nelson T; Myers TW; Veauthier JM; Chavez DE; Scharff RJ; Tretiak S Two-Photon Absorption in Conjugated Energetic Molecules. J. Phys. Chem. A 2016, 120, 4455–4464. [PubMed: 27257984]

(78). Kilina S; Kilin D; Tretiak S Light-Driven and Phonon-Assisted Dynamics in Organic and Semiconductor Nanostructures. Chem. Rev 2015, 15, 5929–5978.

(79). Martin RL Natural Transition Orbitals. J. Chem. Phys 2003, 118, 4775–4777.

(80). Humphrey W; Dalke A; Schulten K VMD: Visual Molecular Dynamics. J. Mol. Graph 1996, 14, 33–38. [PubMed: 8744570]

(81). McCusker CE; Hablot D; Ziessel R; Castellano FN Metal Coordination Induced π-Extension and Triplet State Production in Diketopyrrolopyrrole Chromophores. Inorg. Chem 2012, 51, 7957–7959. [PubMed: 22813434]

(82). McCusker CE; Hablot D; Ziessel R; Castellano FN Triplet State Formation in Homo- and Heterometallic Diketopyrrolopyrrole Chromophores. Inorg. Chem 2014, 53, 12564–12571. [PubMed: 25394202]

(83). Auffrant A; Barbieri A; Barigelletti F; Collin J-P; Flamigni L; Sabatini C; Sauvage J-P Dinuclear Iridium(III) Complexes Consisting of Back-to-Back tpy-(ph)$_n$-tpy Bridging Ligands ($n = 0, 1,$ or 2) and Terminal Cyclometallating Tridentate N-C-N Ligands. Inorg. Chem 2006, 45, 10990–10997. [PubMed: 17173458]

(84). Dubinina GG; Price RS; Abboud KA; Wicks G; Wnuk P; Stepanenko Y; Drobizhev M; Rebane A; Schanze KS Phenylene Vinylene Platinum(II) Acetylides with Prodigious Two-Photon Absorption. J. Am. Chem. Soc 2012, 134, 19346–19349. [PubMed: 23134488]

(85). Liu R; Li Y; Li Y; Zhu H; Sun W Photophysics and Nonlinear Absorption of Cyclometalated 4,6-Diphenyl-2,2′-bipyridyl Platinum(II) Complexes with Different Acetylide Ligands. J. Phys. Chem. A 2010, 114, 12639–12645. [PubMed: 21077600]

(86). Liu R; Dandu N; Li Y; Kilina S; Sun W Synthesis, Photophysics and Reverse Saturable Absorption of Bipyridyl Platinum(II) Bis(arylfluorenylacetylide) Complexes. Dalton Trans. 2013, 42, 4398–4409. [PubMed: 23338679]

(87). Sun Y; Joyce LE; Dickson NM; Turro C Efficient DNA Photocleavage by [Ru(bpy)$_2$(dppn)]$^{2+}$ with Visible Light. Chem. Commun 2010, 46, 2426–2428.

(88). Liu Y; Hammitt R; Lutterman DA; Joyce LE; Thummel RP; Turro C Ru(II) Complexes of New Tridentate Ligands: Unexpected High Yield of Sensitized $^1O_2$. Inorg. Chem 2009, 48, 375–385. [PubMed: 19035764]

(89). Foxon SP; Metcalfe C; Adams H; Webb M; Thomas JA Electrochemical and Photophysical Properties of DNA Metallo-intercalators Containing the Ruthenium(II) Tris(1-pyrazolyl)methane Unit. Inorg. Chem 2007, 46, 409–416. [PubMed: 17279819]

(90). Foxon SP; Alamiry MAH; Walker MG; Meijer AJHM; Sazanovich IV; Weinstein JA; Thomas JA Photophysical Properties and Singlet Oxygen Production by Ruthenium(II) Complexes of Benzo[*i*]dipyrido[3,2-a:2′,3′-c]phenazine: Spectroscopic and TD-DFT Study. J. Phys. Chem. A 2009,113, 12754–12762. [PubMed: 19791785]

(91). Papanikolaou PA; Tkachenko NV Probing the Excited State Dynamics of a New Family of Cu(I)-Complexes with an Enhanced Light Absorption Capacity: Excitation-Wavelength Dependent Population of States Through Branching. Phys. Chem. Chem. Phys 2013, 15, 13128–13136. [PubMed: 23824232]

(92). Blazek ER; Peak JG; Peak MJ Singlet Oxygen Induces Frank Strand Breaks as Well as Alkali- and Piperidine-Labile Sites in Supercoiled Plasmid DNA. Photochem. Photobiol 1989, 49, 607–613. [PubMed: 2755997]
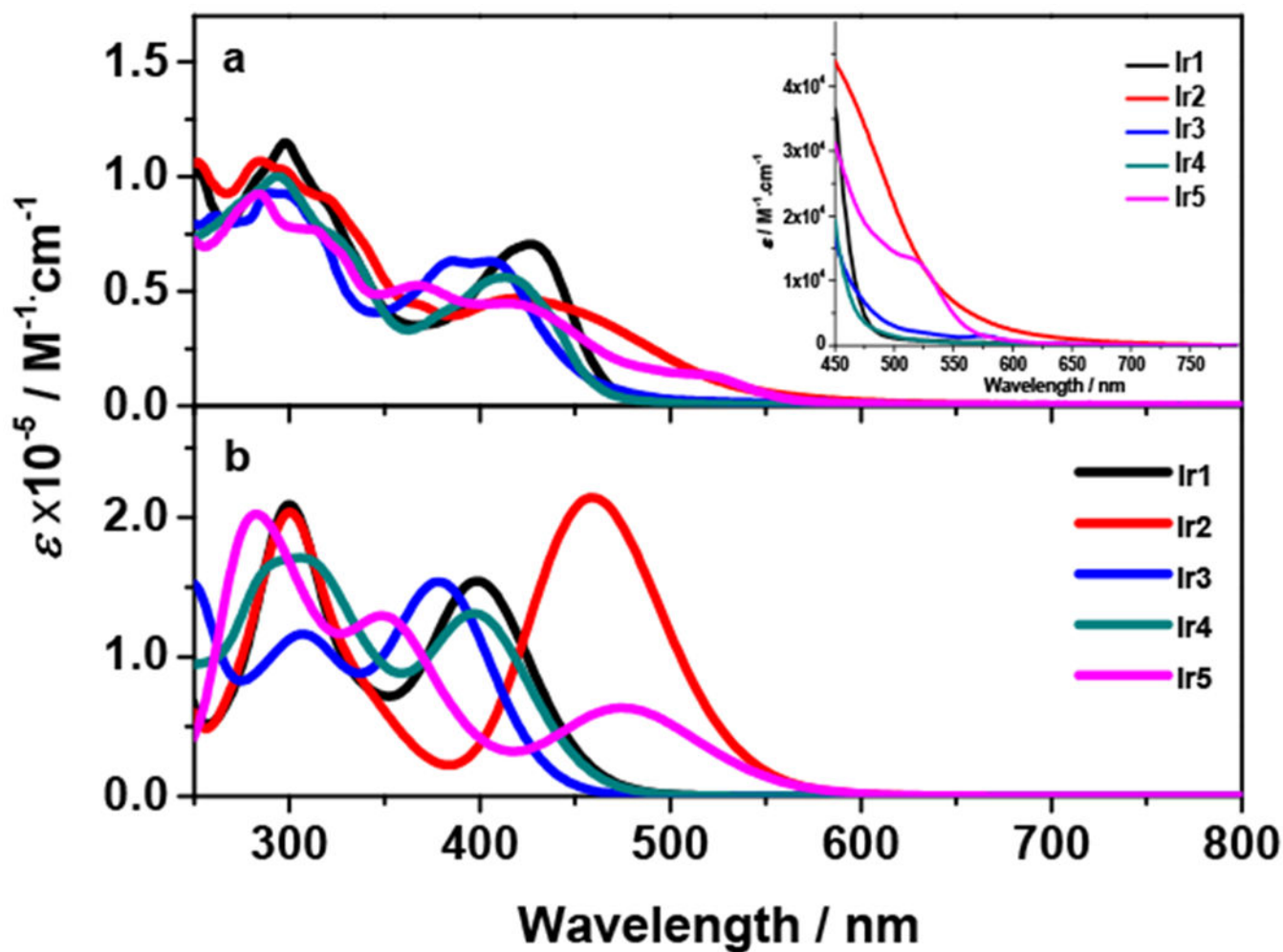
Figure 1.
Experimental (a) and theoretical (b) UV–vis absorption spectra of **Ir1 – Ir5** at room temperature in acetonitrile. The inset in panel (a) is the expansion of the spectra in the region of 450–800 nm. The theoretical spectra were computed using ωB97XD with mixed basis set. A redshift of 0.55 eV for the theoretical spectra in panel (b) was applied for better comparison with the experimental spectra.
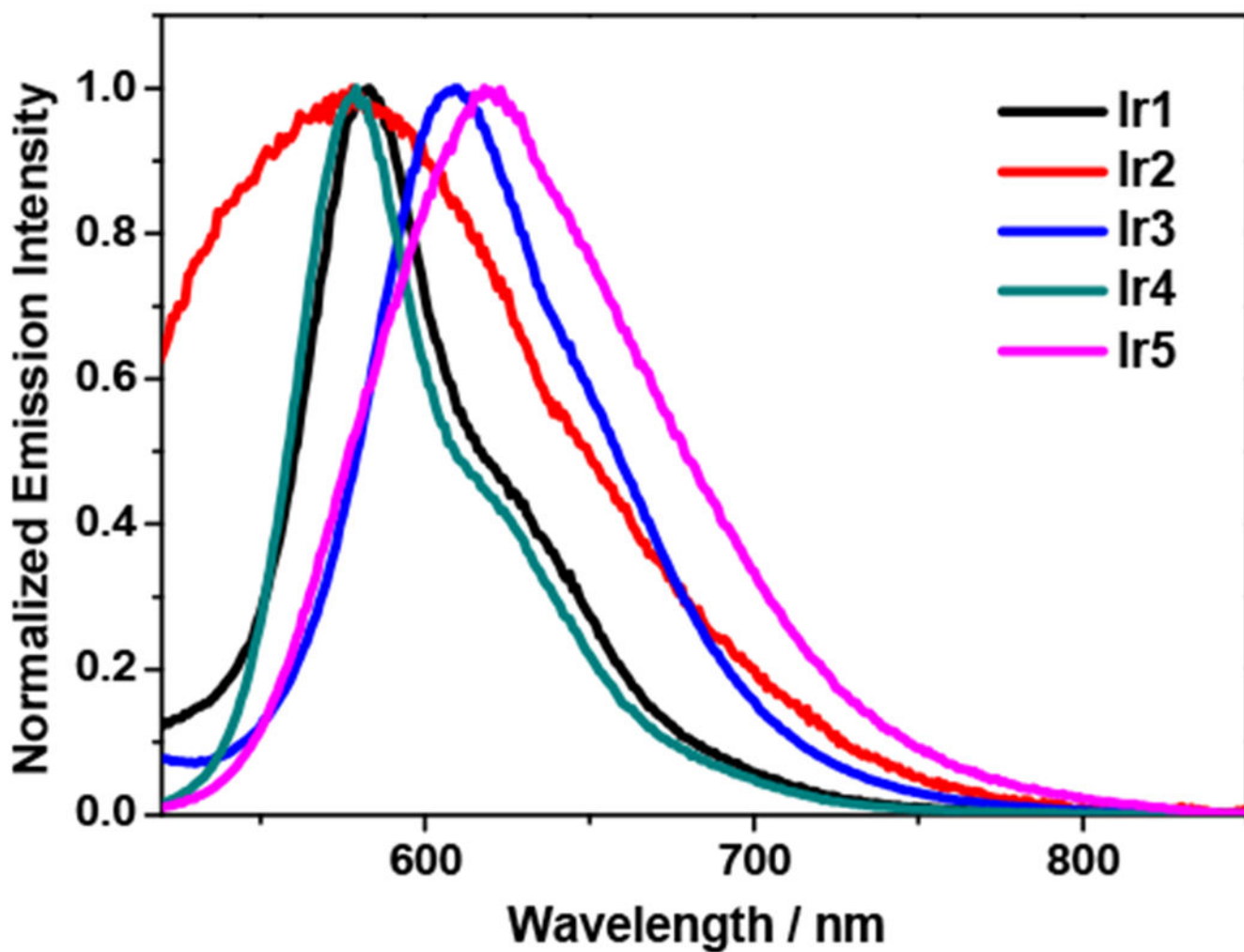
Figure 2.
Experimental emission spectra of **Ir1** (λ_{ex} = 426 nm), **Ir2** (λ_{ex} = 420 nm), **Ir3** (λ_{ex} = 405 nm), **Ir4** (λ_{ex} = 413 nm), and **Ir5** (λ_{ex} = 415 nm) at room temperature in deoxygenated acetonitrile (c = 1×10^{-5} mol·L^{-1}).
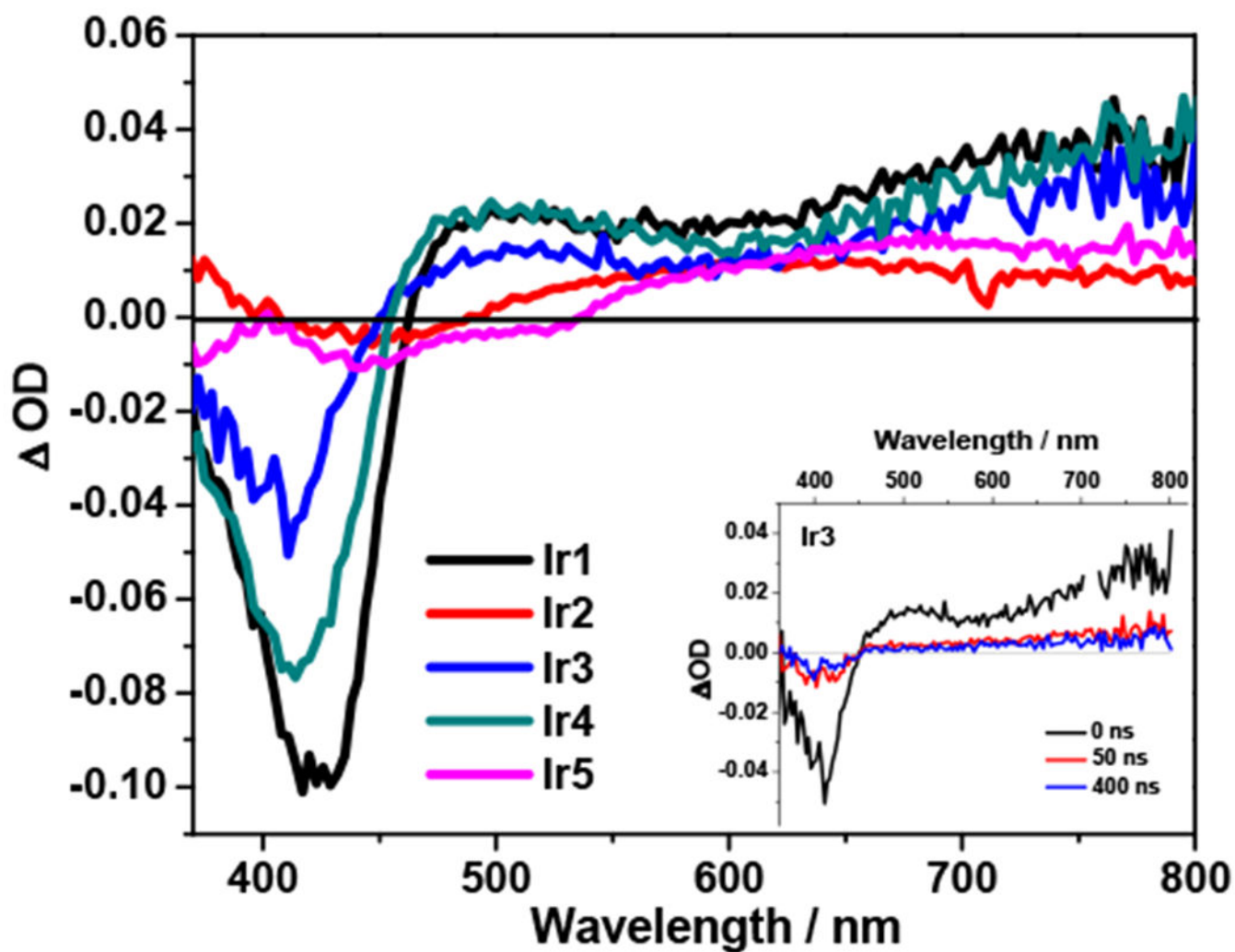
Figure 3.
Nanosecond transient absorption (TA) spectra of complexes **Ir1 – Ir5** in deoxygenated acetonitrile at zero delay after 355 nm excitation. The inset shows the TA spectra of **Ir3** at different delay time after excitation. $A_{355\,nm} = 0.4$ in a 1-cm cuvette.
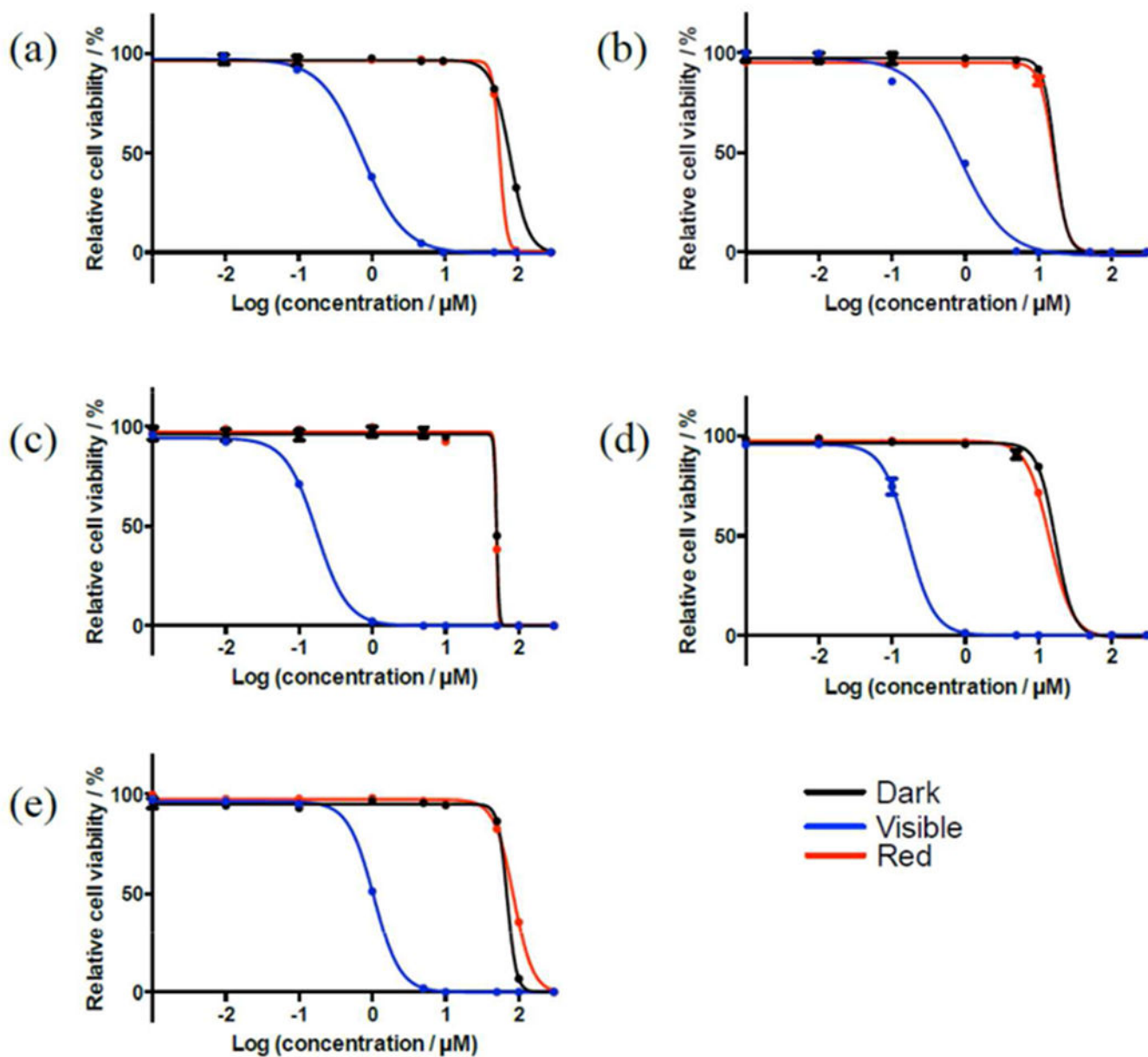
Figure 4.
In vitro dose-response curves for complexes **Ir1** (a), **Ir2** (b), **Ir3** (c), **Ir4** (d), and **Ir5** (e) in SK-MEL-28 cells treated in the dark (black) and with visible (blue) or red (red) light activation.
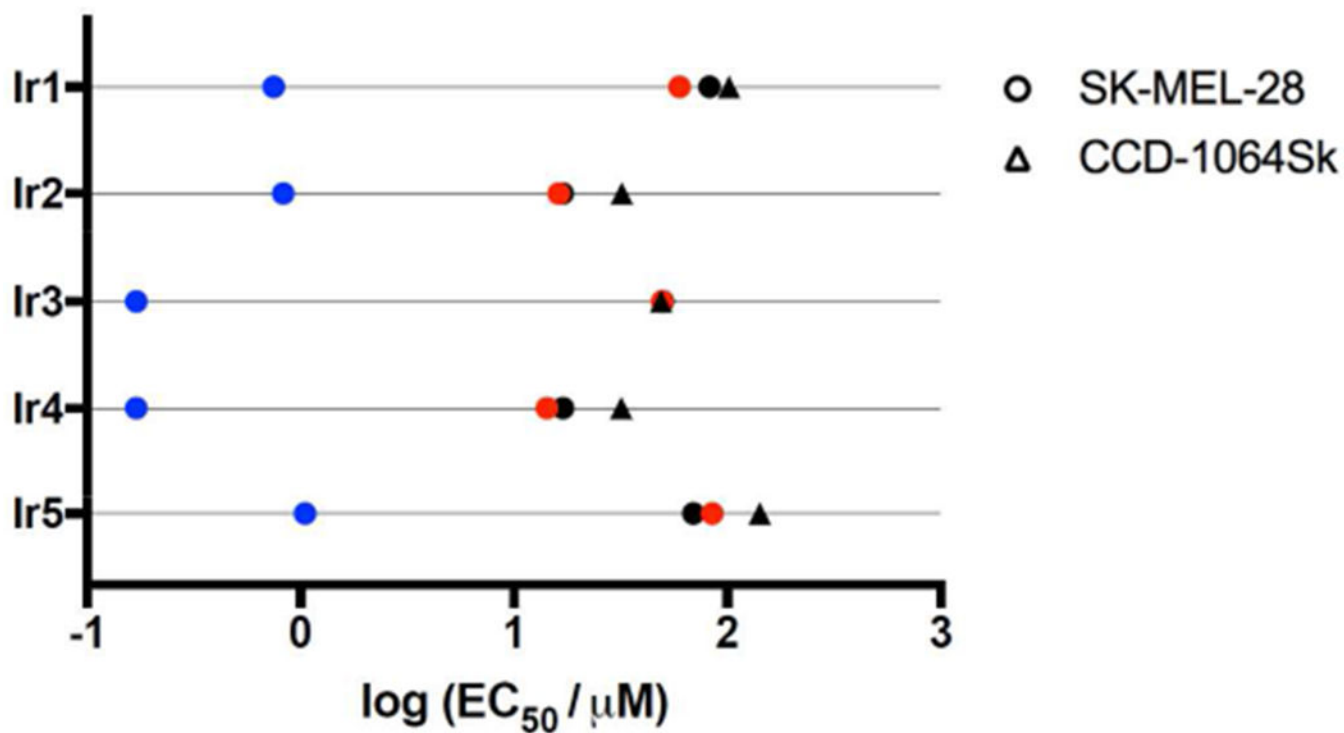
Figure 5.
Activity plot for complexes **Ir1 - Ir5** in SK-MEL-28 and CCD-1064Sk cells treated in the dark (black) and with visible (blue) or red (red) light activation.
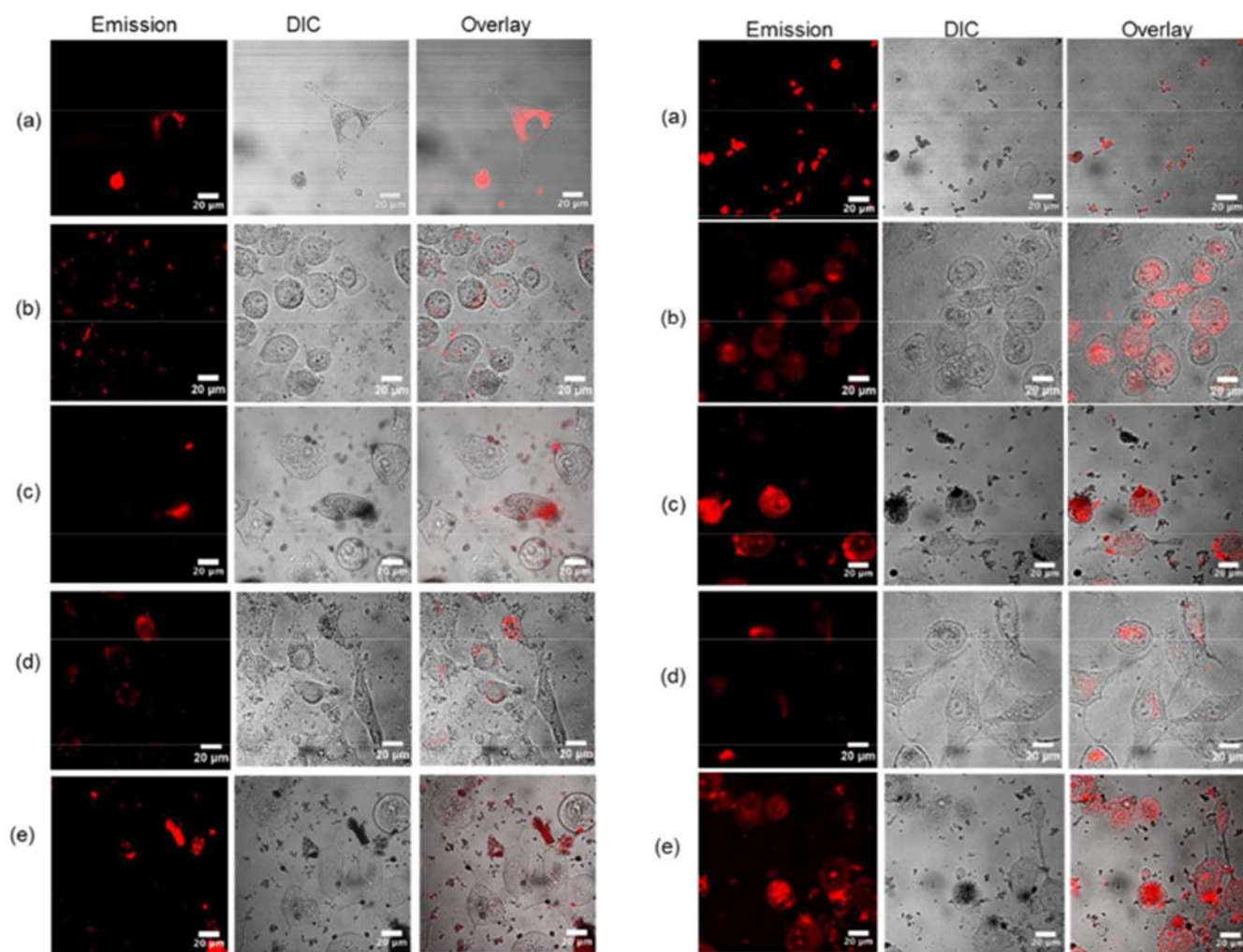
Figure 6.
Confocal luminescence images of SK-MEL-28 cells dosed with **Ir1 - Ir5** (a-e, 50 μM) in the dark (left) and with visible light (50 J·cm^{-2}) (right).
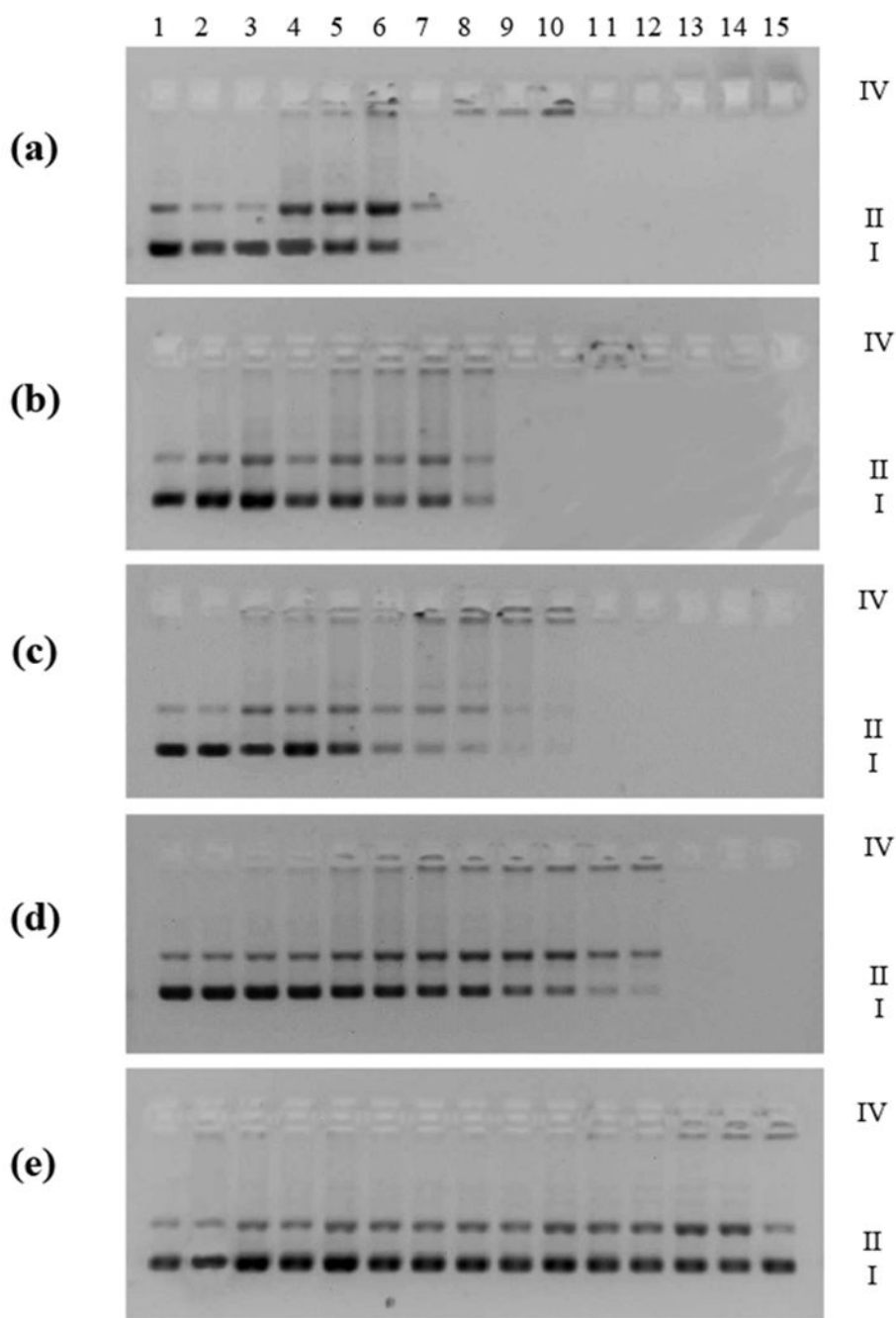
Figure 7.
DNA photocleavage of pUC19 DNA (20 μM) dosed with metal complex (MC) **Ir1** (a), **Ir2** (b), **Ir3** (c), **Ir4** (d), **Ir5** (e) and visible light (14 J·cm^{-2}). Gel mobility shift assays employed 1% agarose gels (0.75 μg·mL^{-1} ethidium bromide) electrophoresed in 1× TAE at 8 V·cm^{-1} for 30 min. Lane 1, DNA only (−hv); lane 2, DNA only (+hv); lane 3, 0.5 μM MC (+hv); lane 4, 1 μM MC (+hv); lane 5, 2 μM MC (+hv) lane 6, 3 μM MC (+hv) lane 7, 5 μM MC (+hv) lane 8, 8 μM MC (+hv); lane 9, 10 μM MC (+hv) lane 10, 12 μM MC (+hv) lane 11, 15 μM MC (+hv) lane 12, 20 μM MC (+hv); lane 13, 50 μM MC (+hv); lane 14, 100 μM

MC ($+hv$); lane 15, 100 μM MC ($-hv$). Forms I, II and IV DNA refer to supercoiled plasmid, nicked circular plasmid, and aggregated plasmid, respectively.
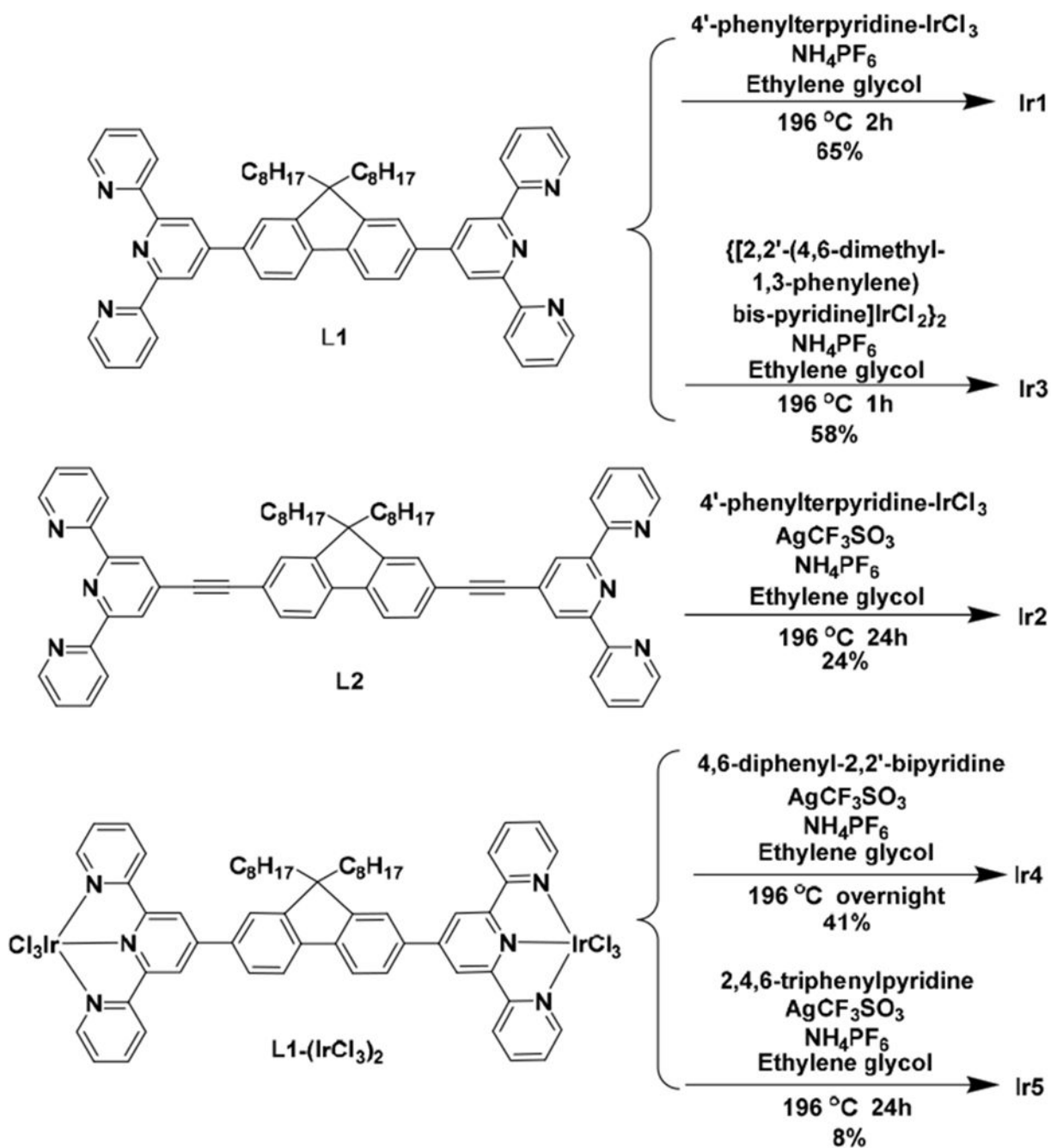
Scheme 1.
Synthetic routes for complexes **Ir1 - Ir5**.
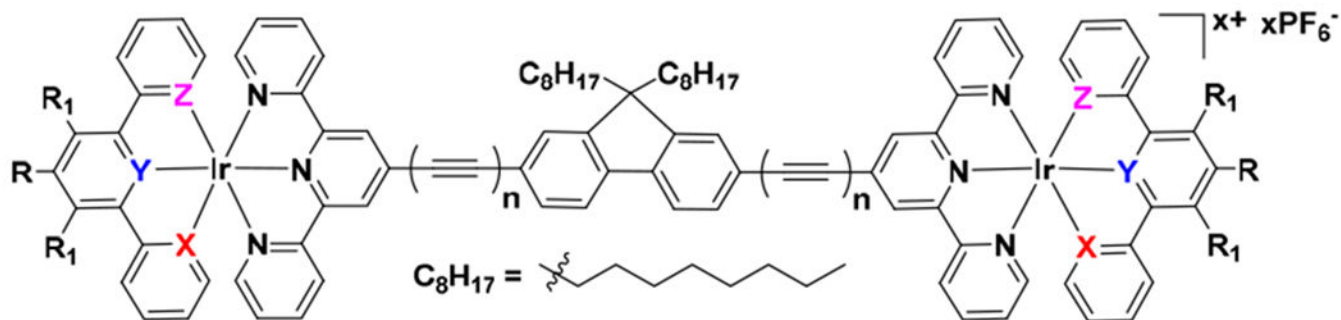
Chart 1.
The molecule structure of target dinuclear Ir(III) complexes

Table 1.

Electronic Absorption, Emission, and Triplet Excited-State Absorption Parameters, as well as Singlet Oxygen Quantum Yields for Complexes Ir1 - Ir5

	λ_{abs}/nm (log ε)[a]	λ_{em}/nm (τ_{em}/μs); Φ_{em}[b]	$\lambda_{T1\text{-}Tn}$/nm (τ_{TA}/μs; log $\varepsilon_{T1\text{-}Tn}$); Φ_T[c]	Φ[d] (λ_{ex}/nm)
Ir1	251 (5.01), 297 (5.06), 427 (4.85)	583 (3.57); 0.024	498 (3.09; -), 765 (3.05; 4.62); 0.44	0.28 (430)
Ir2	251 (5.03), 285 (5.03), 364 (4.65), 420 (4.68)	576 (1.99); 0.003	385 (1.72; -), 640 (1.75; 5.04); 0.03	0.26 (468)
Ir3	260 (4.92), 289 (4.97), 386 (4.80), 405 (4.80)	608 (1.47); 0.025	513 (0.03 (17%), 1.72 (83%); -), 770 (0.03 (15%), 1.75 (85%)); 4.70); 0.14	0.04 (411)
Ir4	294 (5.00), 321 (4.88), 413 (4.75)	578 (53.3); 0.22	498 (48.6; -), 800 (48.3; 4.64); 0.28	0.38 (418)
Ir5	283 (4.97), 312 (4.89), 368 (4.72), 416 (4.65), 520 (4.13)	619 (1.92); 0.045	681 (2.68; 4.80), 787 (2.68; -); 0.07	0.22 (418)

[a]Absorption band maxima (λ_{abs}) and molar extinction coefficients (ε / L·mol^{-1}·cm^{-1}) of the UV-vis absorption in acetonitrile at room temperature.

[b]Emission band maxima (λ_{em}), lifetimes (τ_{em}), and quantum yields (Φ_{em}) measured in acetonitrile ($c = 1 \times 10^{-5}$ mol·L^{-1}) at room temperature with Ru(bpy)$_3$Cl$_2$ (in degassed acetonitrile; $\Phi_{em} = 0.097$, $\lambda_{ex} = 436$ nm) as the reference.

[c]Nanosecond TA band maxima ($\lambda_{T1\text{-}Tn}$), triplet excited-state lifetimes (τ_{TA}), triplet molar extinction coefficients ($\varepsilon_{T1\text{-}Tn}$ / L·mol^{-1}·cm^{-1}), and quantum yields for triplet state formation (Φ_T) measured in acetonitrile at room temperature with SiNc (in degassed benzene; $\varepsilon_{590} = 70,000$ L·mol^{-1}·cm^{-1}, $\Phi_T = 0.20$) as the reference. $\lambda_{ex} = 355$ nm.

[d]Singlet oxygen quantum yields in acetonitrile. Values are correct to within ±5%.

Table 2.

Natural Transition Orbitals (NTOs) for Low Energy Transitions of Ir1 - Ir5. For Transitions with Quasi-Degenerate Transition Orbitals, Only One Pair of Transition Densities Are Shown and Are Indicated By *.
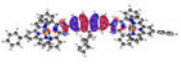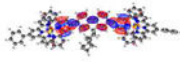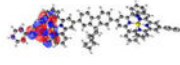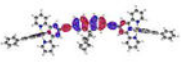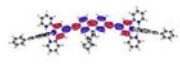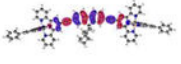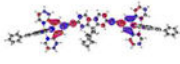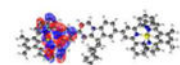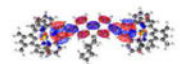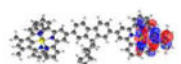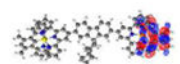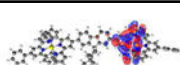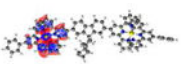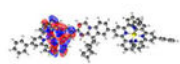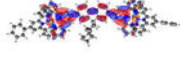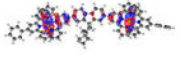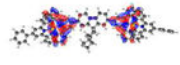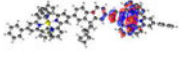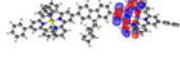
	S_n	Hole	Electron
Ir1	S_1 340 nm f = 2.637		
	S_5 303 nm f = 0.109		
Ir2	S_1 381nm f = 3.730		
	S_2* 336 nm f = 0.079		
Ir3	S_1 333 nm f = 0.010		
	S_3 328 nm f = 2.189		
	S_7 311 nm f = 0.368		
Ir4	S_1 351 nm f = 0.003		
	S_2 350 nm f = 0.004		
	S_3* 340 nm f = 2.002		
Ir5	S_1* 395 nm f = 0.933		
	S_6* 372 nm f = 0.050		

Table 3.

Comparison of EC$_{50}$ values (μM) for SK-MEL-28 cancer cells and CCD-1064Sk normal skin fibroblasts dosed with complexes **Ir1 – Ir5.**

		SK-MEL-28 cells				CCD-1064Sk cells	
	Dark	Vis[a]	PI[b]	Red[c]	PI[d]	Dark	SF[e]
Ir1	82.6 ± 1.5	0.75 ± 0.01	111	59.7 ± 0.4	1.4	102 ± 2	1.2
Ir2	16.9 ± 0.8	0.83 ± 0.05	20	16.2 ± 0.5	1.0	32.0 ± 2.0	1.9
Ir3	49.9 ± 0.1	0.17 ± 0.01	288	49.5 ± 0.1	1.0	49.1 ± 0.1	1.0
Ir4	17.0 ± 0.7	0.17 ± 0.01	102	14.3 ± 0.3	1.2	31.8 ± 1.8	1.9
Ir5	69.5 ± 1.0	1.05 ± 0.01	66	85.1 ± 1.0	0.82	142 ± 3	2.0

[a]Vis-PDT: 16 hours drug-to-light interval followed by 100 J·cm^{-2} broadband visible light irradiation

[b]PI = phototherapeutic index (ratio of dark EC$_{50}$ to visible-light EC$_{50}$)

[c]Red-PDT: 16 hours drug-to-light interval followed by 100 J·cm^{-2} light irradiation with 625-nm LEDs

[d]PI = phototherapeutic index (ratio of dark EC$_{50}$ to red-light EC$_{50}$)

[e]SF SK-MEL-28: selectivity factor (ratio of dark CCD-1064Sk EC$_{50}$ to dark SK-MEL-28 EC$_{50}$).